UC San Diego
UC San Diego Electronic Theses and Dissertations

Title

Computational Analysis of Biventricular Shape and Mechanics in Tetralogy of Fallot: Discovering Atlas-Based Biomarkers to Aid Clinical Prognosis

Permalink

https://escholarship.org/uc/item/63p0z1js

Author

Govil, Sachin

Publication Date

2023

Peer reviewed|Thesis/dissertation

UNIVERSITY OF CALIFORNIA SAN DIEGO

Computational Analysis of Biventricular Shape and Mechanics in Tetralogy of Fallot:
Discovering Atlas-Based Biomarkers to Aid Clinical Prognosis

A dissertation submitted in partial satisfaction of the
requirements for the degree Doctor of Philosophy

in

Bioengineering

by

Sachin Govil

Committee in charge:

Professor Andrew D. McCulloch, Chair
Professor Sanjeet Hegde
Professor Kevin R. King
Professor Elliot R. McVeigh
Professor Jeffrey H. Omens
Professor James C. Perry

2023

The Dissertation of Sachin Govil is approved, and it is acceptable in quality and

form for publication on microfilm and electronically.

University of California San Diego

2023

DEDICATION

This dissertation is dedicated to my beloved parents, Dr. Sanjay Govil and Mrs. Meenakshi

Govil, and my wonderful big brother, Sagar Govil, for their endless love, support, and

encouragement in my pursuit of higher education and endless exploration.

EPIGRAPH

In general, in life, it is about input with not knowing the outcome.

To invest EVERYTHING and not be sure what the outcome would be,

This is what makes life interesting∼

TT

TABLE OF CONTENTS

LIST OF FIGURES

ACKNOWLEDGEMENTS

I would like to acknowledge and thank my primary advisors, Dr. Andrew McCulloch and Dr. Jeff Omens, for their mentorship and guidance in becoming an independent researcher and scientist. Their feedback has been invaluable for helping define my research trajectory and execute my research aims. I would also like to acknowledge my clinical advisors, Dr. Jim Perry and Dr. Sanjeet Hegde, for helping keep my research goals grounded in having real clinical impact. Their involvement and interest in the work I was doing was always a source of inspiration and motivation to push the boundaries of clinical translational research. I am also grateful to Dr. Elliot McVeigh and Dr. Kevin King for serving on my dissertation committee.

I would also like to acknowledge many others, who without their help, none of this work would be possible. I am extremely grateful to Dr. Alistair Young for being an open and communicative collaborator with respect to sharing clinical datasets, modeling tools, and analysis techniques. I would also like to thank Dr. Kevin Vincent and Dr. Nick Forsch for training me on many of the computational tools employed here, for always taking the time to answer all of my questions, and for being amazing mentors and role-models not only for research but for life in general. I am also grateful to the staff at Rady Children's Hospital San Diego, notably Dr. Xiaoyang Yu and Fernando Ramirez, for assisting with clinical data acquisition.

I would like to acknowledge members of the Cardiac Mechanics Research Group for making the lab an enjoyable and engaging workplace. I would like to give a huge shoutout to Swithin Razu, Joe Powers, Ariel Wang, Abby Teitgen, and Marcus Hock for cultivating a genuine camaraderie that extends beyond the walls of the lab. I am so thankful for all of your support through the challenges and difficulties of graduate school and for always listening to what I had to say. I would also like to thank Jen Stowe for making the administrative part of graduate school as simple as possible and for always greeting me with a smile and a warm conversation.

I would like to acknowledge my family, Mom, Dad, and Sagar, for their unconditional love and support throughout this entire journey. The three of you have known me my whole life and have been integral in shaping the person I am today. Thank you for always taking good care

of me and encouraging me to follow my own path. I am also very grateful to my friends – I have always felt so fortunate to be surrounded by so many good people in all walks of my life. Thank you for all the memories we have shared together.

Finally, I would like to acknowledge all of the individuals affected by congenital heart defects and who contributed their health data to the work presented in this dissertation. We do all of this so that they can live longer and healthier lives.

The Introduction, in part, is a reprint of the material as it appears in the following article: Forsch N, Govil S, Perry JC, Hegde S, Young AA, Omens JH, McCulloch AD. Computational analysis of cardiac structure and function in congenital heart disease: Translating discoveries to clinical strategies. *Journal of Computational Science*. (2020). The dissertation author is the second author of this paper.

Chapter 1, in full, is a reprint of the material as it appears in the following article: Govil S*, Crabb BT*, Deng Y, Toso LD, Puyol-Anton E, Pushparajah K, Hegde S, Perry JC, Omens JH, Hsiao A, Young AA, McCulloch AD. A Deep Learning Approach for Fully Automated Cardiac Shape Modeling in Tetralogy of Fallot. *Journal of Cardiovascular Magnetic Resonance*. (2023). The dissertation author is the co-first author of this paper.

Chapter 2, in full, is a reprint of the material as it appears in the following article: Govil S*, Mauger CA*, Hegde S, Occleshaw CJ, Yu X, Perry JC, Young AA, Omens JH, McCulloch AD. Biventricular Shape Modes Discriminate Pulmonary Valve Replacement in Tetralogy of Fallot Better Than Imaging Indices. *Scientific Reports*. (2023). The dissertation author is the co-first author of this paper.

Chapter 3, in full, is a reprint of the material as it appears in the following article: Govil S, Hegde S, Perry JC, Omens JH, McCulloch AD. An Atlas-Based Analysis of Biventricular Mechanics in Tetralogy of Fallot. *STACOM 2022 International Workshop on Statistical Atlases and Computational Models of the Heart*. (2022). The dissertation author is the first author of this paper.

VITA

2017   Bachelor of Science, Duke University

2018   Master of Science, Duke University

2023   Doctor of Philosophy, University of California San Diego

PUBLICATIONS

Pankewitz L, Hustad KG, **Govil S**, Perry JC, Hegde S, Tang R, Omens JH, Young AA, McCulloch AD, Arevalo HJ. CobivecoX - Development of a biventricular coordinate system with representation of an anatomically detailed base. *Medical Image Analysis*. (In Review)

Crabb BT, Chandrupatla RS, Masutani EM, You S, **Govil S**, Montserrat S, Prat-Gonzalez S, Vega-Adauy J, Atkins M, Lorenzatti D, Zocchi C, Panaioli E, Alshawabkeh L, Hahn L, Hegde S, McCulloch AD, Raimondi F*, Hsiao A*. Deep Learning Analysis and Unsupervised Clustering of Left Ventricular Mechanics in Tetralogy of Fallot. *Journal of Cardiovascular Magnetic Resonance*. (In Review)

Govil S*, Crabb BT*, Deng Y, Toso LD, Puyol-Anton E, Pushparajah K, Hegde S, Perry JC, Omens JH, Hsiao A, Young AA, McCulloch AD. A Deep Learning Approach for Fully Automated Cardiac Shape Modeling in Tetralogy of Fallot. *Journal of Cardiovascular Magnetic Resonance*. (2023)

Govil S*, Mauger CA*, Hegde S, Occleshaw CJ, Yu X, Perry JC, Young AA, Omens JH, McCulloch AD. Biventricular Shape Modes Discriminate Pulmonary Valve Replacement in Tetralogy of Fallot Better Than Imaging Indices. *Scientific Reports*. (2023)

Govil S, Hegde S, Perry JC, Omens JH, McCulloch AD. An Atlas-Based Analysis of Biventricular Mechanics in Tetralogy of Fallot. *STACOM 2022 International Workshop on Statistical Atlases and Computational Models of the Heart*. (2022)

Tang R, **Govil S**, Mauger CA, Hegde S, Omens JH, Perry JC, McCulloch AD. Modeling Single Ventricle Morphology With a HLHS-Specific Biventricular Template to Enhance Statistical Shape and Biomechanics Analyses. *ASME 2022 International Mechanical Engineering Congress and Exposition*. (2022)

Crabb BT, **Govil S**, Hegde S, Perry JC, Young AA, Omens JH, Kim NH, Valdez-Jasso D, Contijoch F. Biventricular Statistical Shape Atlas of Unloaded Reference Geometries: A Novel Method to Control for Hemodynamic Variations in End-Diastolic Pressure. *ASME 2022 International Mechanical Engineering Congress and Exposition*. (2022)

Elsayed A, Mauger CA, Ferdian E, Gilbert K, Scadeng M, Occleshaw CJ, Lowe BS, McCulloch AD, Omens JH, **Govil S**, Pushparajah K, Young AA. Right Ventricular Flow Vorticity Relationships With Biventricular Shape in Adult Tetralogy of Fallot. *Frontiers in Cardiovascular Medicine*. (2022)

Govil S*, Forsch N*, Salehyar S, Gilbert K, Suinesiaputra A, Hegde S, Perry JC, Young AA, Omens JH, McCulloch AD. Morphological Markers and Determinants of Left Ventricular Systolic Dysfunction in Repaired Tetralogy of Fallot. *ASME 2021 International Mechanical Engineering Congress and Exposition*. (2021)

Mauger CA*, **Govil S***, Chabiniok R, Gilbert K, Hegde S, Hussain T, McCulloch AD, Occleshaw CJ, Omens JH, Perry JC, Pushparajah K, Suinesiaputra A, Zhong L, Young AA. Right-Left ventricular shape variations in tetralogy of Fallot: associations with pulmonary regurgitation. *Journal of Cardiovascular Magnetic Resonance*. (2021)

Vincent KP, Forsch N, **Govil S**, Joblon JM, Omens JH, Perry JC, McCulloch AD. Atlas-based methods for efficient characterization of patient-specific ventricular activation patterns. *Europace*. (2021)

Forsch N, **Govil S**, Perry JC, Hegde S, Young AA, Omens JH, McCulloch AD. Computational analysis of cardiac structure and function in congenital heart disease: Translating discoveries to clinical strategies. *Journal of Computational Science*. (2020)

Narayan HK, Xu R, Forsch N, **Govil S**, Iukuridze D, Lindenfeld L, Adler E, Hegde S, Tremoulet A, Ky B, Armenian S, Omens JH, McCulloch AD. Atlas-based measures of left ventricular shape may improve characterization of adverse remodeling in anthracycline-exposed childhood cancer survivors: A cross-sectional imaging study. *Cardio-Oncology*. (2020)

Govil S, Katz DF. Deducing Mucosal Pharmacokinetics and Pharmacodynamics of the Anti-HIV Molecule Tenofovir from Measurements in Blood. *Scientific Reports*. (2019)

FIELDS OF STUDY

Major Field: Bioengineering

ABSTRACT OF THE DISSERTATION

Computational Analysis of Biventricular Shape and Mechanics in Tetralogy of Fallot:
Discovering Atlas-Based Biomarkers to Aid Clinical Prognosis

by

Sachin Govil

Doctor of Philosophy in Bioengineering

University of California San Diego, 2023

Professor Andrew D. McCulloch, Chair

Tetralogy of Fallot (TOF) is the most common cyanotic congenital heart disease accounting for about 10% of all congenital cardiac malformations. Due to improvements in surgical technique, individuals with repaired TOF (rTOF) are surviving into adulthood but face residual pulmonary regurgitation that can lead to adverse ventricular remodeling and, ultimately, heart failure. Cardiovascular magnetic resonance (CMR) imaging is the gold standard for evaluation in patients with rTOF, but the wealth of information available in CMR images is under-utilized. We sought to use computational tools to extract atlas-based biomarkers of regional biventricular shape and mechanics from standard of care CMR images to better aid clinical management

of rTOF. Specifically, the aims of this dissertation were to 1) rapidly build biventricular shape models from CMR data using machine learning; 2) formulate shape atlases from these models to identify clinically meaningful shape variation within the population; and 3) construct biventricular biomechanics models to quantify shape marker relationships with differences in myocardial mechanical properties. Herein we demonstrate a fully automated, end-to-end pipeline that can robustly create biventricular shape models for the challenging anatomies present in rTOF. We also discovered specific markers of biventricular shape that are better discriminators of clinical prognosis than standard imaging indices. These markers of biventricular shape were also partial determinants of systolic function and may also be surrogate measures for altered myocardial contractility. Overall, patients with rTOF may benefit from routine atlas-based analyses of biventricular shape and mechanics that can supplement clinical decision making and provide insight into mechanisms underlying myocardial pathophysiology.

Introduction

The wide-scale availability of large, heterogeneous patient datasets brings new opportunities to tackle complex problems in clinical medicine. In the field of cardiology, advances in cardiovascular imaging have the potential to enable more quantitative approaches to diagnosis, surgical planning, and medical therapies, but much of the information in cardiac imaging data goes under-utilized by routine clinical assessment methods. In diagnostics, cardiac magnetic resonance (CMR) imaging is not routine in acquired heart diseases but is common in congenital heart diseases (CHDs), where patients are often very young and repeated exposure to ionizing radiation is contraindicated. Improved availability of clinical datasets for research is accelerating the intersection of medicine and computational science, fostering collaborations within and between the biomedical sciences, computational sciences, and clinical communities. Through these collaborations, anecdotal and empirical clinical practice is evolving towards evidence-based precision medicine. In this chapter, we provide background on tetralogy of Fallot (TOF), the most common form of cyanotic CHD, and discuss the breadth of clinical challenges and research strategies related to the clinical management of individuals with TOF.

0.1   Tetralogy of Fallot

Tetralogy of Fallot is the most common cyanotic CHD occurring in approximately 4-5 per 100,000 live births and accounting for about 7-10% of all congenital cardiac malformations [1, 2]. The anatomy of TOF, which is composed of four defects including an overriding aorta, pulmonary valve stenosis, a ventricular septal defect (VSD), and right ventricular (RV) hypertrophy, was

extensively described by the French physician Étienne-Louis Fallot in 1888 [3]. There are several different phenotypes of TOF that include additional anatomical abnormalities, such as TOF with pulmonary atresia or TOF with double outlet right ventricle. These phenotypes are much more severe and may require different management and treatment strategies. In this overview and in the studies presented in this dissertation, we focus on the "classic" TOF shown in Figure 0.1.

0.2   Surgical Management

The surgical approach to TOF repair has evolved considerably since it was first described by Lillehei et al. in 1955 [4], but the primary objectives of closing the VSD and widening the narrowed pulmonary outflow tract remain the same. Historically, surgical repair was conducted via a ventriculotomy approach with aggressive right ventricular outflow tract (RVOT) obstruction relief. However, follow-up studies of these initial operations showed that residual lesions from this approach were common and resulted in late morbidity and mortality [5, 6, 7, 8]. In the modern era, surgical repair is conducted via a transatrial or transatrial-transpulmonary approach to try and preserve competence of the pulmonary valve with acceptance of some degree of residual RVOT obstruction. Follow up studies of these operations demonstrated that this approach has excellent long-term outcomes [9, 10, 11]. In both of these cases, the widening of the narrowed pulmonary outflow tract is commonly achieved by performing a transannular patch repair. However, more recently, other techniques have been used to either preserve pulmonary valve competence, such as through pulmonary valvuloplasty [12, 13], or replace the pulmonary valve entirely, including implantation of a monocusp valve [14], a valved right ventricle-to-pulmonary artery conduit [15, 16], or a homograft valve [16]. Typically, complete intracardiac repair is performed in the first year of life; however, in cases where the neonate is unable to undergo complete repair, a palliative systemic-to-pulmonary artery shunt is placed to allow time for the pulmonary artery to grow before conducting complete repair at a later time [17].

0.3 Consequences of Repair

Due to these advancements in surgical technique and perioperative care, complete surgical repair of TOF has resulted in a twenty-five-year mortality rate of only 5% [18], and there is now a large and growing population of adults with repaired TOF (rTOF) who require lifelong specialized medical care [19, 20]. This care includes monitoring for long-term sequelae, including pulmonary regurgitation (PR), that can lead to RV volume overload [21, 22, 23]. Over time, chronic pulmonary valve insufficiency and RV volume overload result in adverse RV remodeling and declining RV and left ventricular (LV) function that are precursors to exercise intolerance and arrhythmias [24, 25]. If the volume load is not eliminated or reduced, RV compensatory mechanisms may eventually fail leading to heart failure and sudden cardiac death [26]. As the adult rTOF population ages, the incidence of heart failure increases, but the characteristics of heart failure in rTOF significantly differ from those in commonly acquired heart failure [26], and may go unrecognized [27].

0.4 Pulmonary Valve Replacement

The strategy for preserving RV function in rTOF relies on surgical or transcatheter pulmonary valve replacement (PVR) to restore pulmonary valve competence and reduce RV volume overload [28]. Ideally, the optimal timing of PVR must strike a balance between being timed early enough to prevent irreversible adverse remodeling, but late enough to reduce the number of re-interventions and potential surgical complications [29]. Because of the difficulties involved in assessing and predicting progressive RV dysfunction, however, the optimal timing of PVR is controversial. The European Society of Cardiology, the Canadian Cardiovascular Society, and the American College of Cardiology / American Heart Association provide recommendations on indications for performing PVR [30, 31, 32], but they are largely qualitative in nature without consensus characterizations, e.g. moderate to severe RV dysfunction, with few quantitative descriptors based on global measures of cardiac mass/volume, e.g. RV end-diastolic volume

3

index greater than 170 mL/m^2. Other global measures of cardiac function, including RV mass-to-volume ratio and RV end-systolic volume index, have also been proposed as thresholds for predictors of outcomes [33]. These guidelines differ between recommending institutions, however, and have several limitations including that they neglect differences between genders and do not account for age differences since the time of initial repair [34], which has since shifted to earlier timepoints in current clinical practice. Therefore, it stands to reason that the decision and timing of PVR would greatly benefit from more detailed and mechanistic-based criteria. Additionally, as RV-LV interactions may play an important role in physiology and prognosis [35, 36], incorporating a quantitative biventricular assessment would be beneficial.

0.5 Clinical Assessment

CMR imaging is the gold standard for evaluation in patients with rTOF, enabling detailed regional analysis of geometry and function [37, 38]. In spite of the wealth of information available from a single CMR image dataset, its value towards clinical decision-making has limitations. Assessment of medical image data requires specialized technical personnel, accurate and reliable software to analyze images, and time to perform the analysis and interpret the results. Additionally, current standards for the quantitative assessment of cardiac structure and function have been under-utilized for prognostic purposes. It is clear that clinical practice surrounding the treatment and management of rTOF could benefit from the translation of computational tools that: 1) accelerate the process of extracting relevant information from image data; 2) condense complex cardiac features into interpretable and quantifiable measures; and 3) provide new insight into disease mechanisms and clinical outcome predictors.

0.6 Aims of the Dissertation

In this dissertation, we ask the question: Can we discover novel atlas-based biomarkers of regional biventricular shape and mechanics from standard of care CMR images that are

better predictors of clinical prognosis than standard imaging indices and that provide a deeper understanding of biventricular remodeling patterns and mechanisms in rTOF? In order to address this question, we use computational tools, i.e. machine learning models, statistical shape models, and finite element biomechanics models, to extract, identify, and quantify salient features of biventricular remodeling and assess their prognostic value. Specifically, the goals of this dissertation were to 1) extract regional morphological information from CMR data to rapidly build biventricular shape models; 2) formulate shape atlases from these models to identify clinically meaningful shape variation within the population; and 3) construct biventricular biomechanics models to quantify shape marker relationships with differences in myocardial mechanical properties. The overall aim of this dissertation was to demonstrate the clinical utility of computational modeling and atlas-based analyses for aiding clinical management of rTOF and providing insight into disease mechanisms. Ultimately, we hope this precision medicine-based approach can serve as a valuable clinical tool that can improve diagnosis, prognosis, and treatment of individuals with TOF and other cardiac diseases.

0.7 Acknowledgments

Figure 0.1. Anatomy of tetralogy of Fallot.

Chapter 1

A Deep Learning Approach for Fully Automated Cardiac Shape Modeling in Tetralogy of Fallot

1.1 Abstract

Cardiac shape modeling is a useful computational tool that has provided quantitative insights into the mechanisms underlying dysfunction in heart disease. The manual input and time required to make cardiac shape models, however, limits their clinical utility. Here we present an end-to-end pipeline that uses deep learning for automated view classification, slice selection, phase selection, anatomical landmark localization, and myocardial image segmentation for the automated generation of three-dimensional, biventricular shape models. With this approach, we aim to make cardiac shape modeling a more robust and broadly applicable tool that has processing times consistent with clinical workflows. Cardiovascular magnetic resonance (CMR) images from a cohort of 123 patients with repaired tetralogy of Fallot (rTOF) from two internal sites were used to train and validate each step in the automated pipeline. The complete automated pipeline was tested using CMR images from a cohort of 12 rTOF patients from an internal site and 18 rTOF patients from an external site. Manually and automatically generated shape models from the test set were compared using Euclidean projection distances, global ventricular measurements, and atlas-based shape mode scores. The mean absolute error (MAE) between manually and

automatically generated shape models in the test set was similar to the voxel resolution of the original CMR images for end-diastolic models (MAE=1.9±0.5mm) and end-systolic models (MAE=2.1±0.7mm). Global ventricular measurements computed from automated models were in good agreement with those computed from manual models. The average mean absolute difference in shape mode Z-score between manually and automatically generated models was 0.5 standard deviations for the first 20 modes of a reference statistical shape atlas. Using deep learning, accurate three-dimensional, biventricular shape models can be created reliably. This fully automated end-to-end approach dramatically reduces the manual input required to create shape models, thereby enabling the rapid analysis of large-scale datasets and the potential to deploy statistical atlas-based analyses in point-of-care clinical settings. Training data and networks are available from cardiacatlas.org.

1.2   Background

Advances in computational medicine have enabled more quantitative approaches to characterizing ventricular shape and remodeling in individuals with heart disease. One such approach is the use of cardiac shape modeling to condense complex, multi-dimensional data from standard of care cardiovascular magnetic resonance (CMR) images into statistical atlases of cardiac structure and function [39, 40, 41, 42, 43, 44, 45, 46, 47, 48, 49, 50, 51, 52]. These atlases are composed of interpretable shape and wall motion features that can be important quantitative biomarkers of patient status and outcome and, in turn, aid in prognosis and treatment of disease.

To extract the relevant features of cardiac morphology that are used to build these statistical atlases, several steps are involved (Figure 1.1). Traditionally, most of these have been performed manually, requiring a human analyst to identify relevant view and slice information from a raw CMR image dataset, identify end-diastolic (ED) and end-systolic (ES) phases in the cardiac cycle, label anatomical features such as the left ventricular (LV) apex and valvular

insertion points, and trace endocardial and epicardial contours. This information can then be collated and processed to build three-dimensional, biventricular shape models, including all four valves (aortic, pulmonary, mitral, tricuspid), and used to build atlases of ED, ES, or systolic wall motion (ES-ED) using principal component analysis. Semi-automated methods for image segmentation have been developed that take advantage of guide-point modeling [53, 54, 55, 56], and more recent efforts have focused on using deep learning (e.g., CNNs, FCNs, U-nets, and RNNs) to completely automate image segmentation [57, 58]. Fully manual and even semi-automated techniques, however, are time-consuming and require significant operator expertise to achieve an acceptable level of accuracy. While fully automated methods have made advances in accuracy, they are prone to error for challenging regions of the heart such as the right ventricle (RV) and the complex anatomies of congenital heart disease (CHD) patients.

With improved availability of large, heterogenous clinical datasets and manually annotated models for reference, the major steps involved in constructing three-dimensional, biventricular shape models from raw CMR image datasets for use in statistical atlas-based analyses can be automated. Herein, we detail the use of deep learning for automated view classification, slice selection, phase selection, anatomical landmark localization, and myocardial image segmentation that together provide an end-to-end pipeline for cardiac shape modeling. Moreover, we demonstrate this approach in a multi-institutional, international cohort of patients with repaired tetralogy of Fallot (rTOF) — a patient population with particularly challenging anatomy. The integration of these steps in an automated fashion can significantly reduce the manual input and time required to create shape models, which has been a significant barrier to the clinical application of atlas-based analyses to patient management.

1.3 Methods

1.3.1 Study Population and Data Acquisition

This study used deidentified, retrospective CMR images of patients with repaired tetralogy of Fallot (rTOF) from three clinical centers (Rady Children's Hospital, San Diego, CA, US; The Center for Advanced Magnetic Resonance Imaging, Auckland, NZ; and Evelina Children's Hospital, London, UK) with approval from local institutional review boards via waiver of informed consent (UCSD IRB 201138; HDEC 16/STH/248; and 21/LO/0650, respectively). Labeled CMR images from 123 rTOF patients were contributed from the Cardiac Atlas Project (CAP) database (https://www.cardiacatlas.org) [59] from San Diego and Auckland (internal sites) and were used as the training/validation set to optimize each step in the automated pipeline. A separate test set composed of labeled CMR images from 30 rTOF patients from San Diego (internal site) and London (external site) was used to evaluate the output of the automated pipeline. A flow-diagram summarizing the datasets employed and how they were used to develop the automated pipeline is shown in Figure 1.2. Summary characteristics of the study participants in the training/validation and test sets are shown in Table 1.1. All patients underwent functional CMR examination within the scope of standard clinical practice. CMR acquisition data for study participants in the training/validation and test sets are shown in Table 1.2.

1.3.2 Automated Cardiac Shape Modeling Pipeline Overview

The automated cardiac shape modeling pipeline was developed as a series of five steps for view classification, slice selection, phase selection, anatomical landmark localization, and myocardial image segmentation, respectively. The view classification network was designed to take a raw CMR image dataset and classify views as either two-chamber left (2CH LT), two-chamber right (2CH RT), three-chamber (3CH), four-chamber (4CH), left ventricular outflow tract (LVOT), right ventricular outflow tract (RVOT), short axis (SA), or other. After view classification, optimal and non-optimal slices in the SA stack were characterized through the

slice selection network. Optimal slices were defined as SA slices that range from the LV apex to the mitral and tricuspid base planes, while non-optimal slices were defined as SA slices either below the LV apex or above the mitral and tricuspid base planes. ED and ES phases were then identified from selected SA slices through the phase selection network. ED and ES phases from the 3CH, 4CH, RVOT, and selected SA slices were then provided as inputs to the anatomical landmark localization networks to identify the LV apex, RV inserts, and mitral, tricuspid, aortic, and pulmonary valve inserts on corresponding views. These anatomical landmarks are required for use with previously developed mesh fitting software, as described below. Finally, ED and ES phases from the 2CH LT, 2CH RT, 3CH, 4CH, RVOT, and selected SA slices were segmented using the myocardial image segmentation network from which contour points were extracted for the LV and RV endocardium, epicardium, and septum. The LV papillary muscles and RV trabeculae were included in the blood pool. The extracted contour points and the anatomical landmark points were then converted from image to model coordinates using an affine transformation and fit to a previously developed biventricular subdivision surface template mesh [60, 61] via diffeomorphic non-rigid registration for contour points and landmark registration for anatomical landmark points. An overview of the automated cardiac shape modeling pipeline is detailed in Figure 1.1. Each step in the pipeline was designed to give the user the ability to make manual corrections if necessary.

1.3.3   Technical Specifications, Network Architectures, and Optimization

For each step in the automated pipeline (view classification, slice selection, phase selection, anatomical landmark localization, and myocardial image segmentation), we report technical specifications regarding the dataset and preprocessing, network architecture, and optimization and evaluation. For the development of the view classification, slice selection, phase selection, and anatomical landmark localization networks, we utilized Python v3.6.15 and Tensorflow v2.4 on a machine with an NVIDIA Tesla V100 GPU. For myocardial image segmentation, we utilized Python v3.7.10 and PyTorch v1.8.1 on a machine with an NVIDIA GeForce RTX 3090

GPU. The 123 cases from the CAP database (https://www.cardiacatlas.org) were randomly split at the patient level into 111 training and 12 validation cases (90-10 percent split), with roughly equal cases from each internal site, San Diego and Auckland, in each set (Figure 1.2). For each network detailed below, training cases with appropriate data were used to optimize the network weights, while validation cases with appropriate data were used for hyper parameter tuning and to estimate model performance.

1.3.4 View Classification

Dataset and Preprocessing

Of the 111 cases in the training set, 93 had complete raw CMR studies available (n=18 excluded) and were included in the training of the view classification network. Similarly, 8 of the cases in the validation set had complete raw CMR studies available (n=4 excluded) and were used for validation. Each CMR series was manually classified into one of eight possible view categories: 2CH LT, 2CH RT, 3CH, 4CH, LVOT, RVOT, SA, or other. Prior to training, each CMR image was converted to an 8-bit integer RGB image and resized to 224 x 224 pixels using bicubic interpolation. Images were normalized by zero-centering each color channel with respect to the ImageNet dataset, without scaling. To improve model generalizability, real-time data augmentations were utilized during training including random rotations (+/- 10%), random zooms (+/- 20%), and random translations (+/- 10%).

Network Architecture

For view classification, the convolutional neural network (CNN) architecture ResNet50 was utilized. Feature extraction layers were imported with pretrained weights from the ImageNet dataset. Classification layers consisted of a 2D global average pooling layer followed by a fully connected dense layer with eight output classes and softmax activation.

Optimization and Evaluation

Prior to training, the pretrained weights in the feature extraction layers were frozen. The classification layers were then optimized with a sparse categorical cross entropy loss function for a total of 25 epochs using a batch size of 16 and a stochastic gradient descent optimizer with a learning rate of 0.0001 and momentum of 0.9. Next, the feature extraction layer weights were unfrozen, the learning rate was decreased by a factor of 2, and training was continued for an additional 50 epochs. Following training, view classification performance was assessed using precision, recall, and F1-scores.

1.3.5   Slice Selection

Dataset and Preprocessing

All 111 cases in the training set and all 12 cases in the validation set had available SA stacks and were included for the optimization of a SA slice selection network. SA slices were split into two possible classifications: optimal and non-optimal. Optimal slices were defined as slices that were manually selected for inclusion in the modeling process by users, which typically range from the LV apex to the mitral and tricuspid base planes. Non-optimal slices were defined as slices that were not included in the modeling process by the manual users. Of note, not every slice between the apex and valve planes is required for modeling; as a result, there was considerable variability in which slices were selected as optimal between cases and users. Prior to training, each CMR image was converted to an 8-bit integer RGB image and resized to 224 x 224 pixels using bicubic interpolation. Images were normalized by zero-centering each color channel with respect to the ImageNet dataset, without scaling. To improve model generalizability, real-time data augmentations were utilized during training including random rotations (+/- 30%), random zooms (+/- 20%), and random translations (+/- 10%).

Network Architecture

For slice selection, the CNN architecture ResNet50 was utilized. Feature extraction layers were imported with pretrained weights from the ImageNet dataset. Classification layers consisted of a 2D global average pooling layer followed by a fully connected dense layer with eight output classes and softmax activation.

Optimization and Evaluation

Prior to training, the pretrained weights in the feature extraction layers were frozen. The classification layers were then optimized with a sparse categorical cross entropy loss function for a total of 25 epochs using a batch size of 16 and a stochastic gradient descent optimizer with a learning rate of 0.0001 and momentum of 0.9. Next, the feature extraction layer weights were unfrozen, the learning rate was decreased by a factor of 2, and training was continued for an additional 50 epochs. Following training, slice selection performance was assessed using precision, recall, and F1-scores.

1.3.6   Phase Selection

Dataset and Preprocessing

All 111 cases in the training set and all 12 cases in the validation set were used to optimize the phase selection network. To produce ground-truth labels, the ES phase was manually labeled for each case using a mid-ventricular slice from the SA stack. The ES phase was determined using the LV and defined as the phase when the LV cavity volume was at a minimum. This label was used to produce a normalized Gaussian distribution centered at the ES phase, with a sigma of 4. In this way, a numerical value was assigned to each phase of the cardiac cycle, increasing to 1 during systole and decreasing to 0 during diastole.

Inputs consisted of SA slices ranging from apex to base. For each slice, CMR images from the complete cardiac cycle were utilized, producing a 2D + time input with 30 phases. Cases with less than 30 phases in the SA stack were zero-padded to maintain a consistent input

14

size. Prior to training, each CMR image was converted to an 8-bit integer RGB image and resized to 224 x 224 pixels using bicubic interpolation. Images were normalized by zero-centering each color channel with respect to the ImageNet dataset, without scaling. To improve model generalizability, real-time data augmentations were utilized during training, including resizing to 256 x 256 pixels and randomly cropping back to 224 x 224 pixels, random brightness adjustments (+/- 10%), and random contrast adjustments (+/- 5%). Inputs were also randomly shuffled along the time axis, such that the ground-truth ES phase could occur at any time point in the 30-phase input.

Network Architecture

The phase selection network consisted of a CNN combined sequentially with a long short-term memory (LSTM) network. This network was chosen based on previously published cardiac phase selection networks [62, 63]. The CNN is used to extract image features, while the LSTM encodes temporal information. For the CNN feature extractor, the CNN architecture ResNet50 was utilized. Feature extraction layers were imported with pretrained weights from the ImageNet dataset. The ResNet50 architecture was followed by two LSTM layers and two fully connected dense layers.

Optimization and Evaluation

Prior to training, the pretrained weights in the feature extraction layers were frozen. The LSTM layers were then optimized with a mean squared error loss function for a total of 75 epochs using a batch size of 4 and a stochastic gradient descent optimizer with a learning rate of 0.0005 and momentum of 0.9. Next, the feature extraction layer weights were unfrozen and training was continued for an additional 150 epochs. Following training, ES phase selection performance was assessed using the average absolute frame difference (AAFD) between predictions and manual labels.

1.3.7   Anatomical Landmark Localization

Dataset and Preprocessing

All 111 cases in the training set and all 12 cases in the validation set were used to optimize the anatomical landmark localization networks. From these cases, the 3CH, 4CH, RVOT, and optimal SA slices were selected. Ground truth anatomical landmarks were manually placed throughout the cardiac cycle for each view by an expert analyst using Cardiac Image Modeller (CIM) software (Auckland, NZ) [64]. In the 3CH view, mitral valve inserts and aortic valve inserts were labeled. In the 4CH view, mitral valve inserts, tricuspid valve inserts, and the LV apex were labeled. In the RVOT view, pulmonary valve inserts were labeled. In the SA slices, RV inserts were labeled. Manual point labels were converted to a normalized Gaussian heat map label with a sigma of 12 for all images. Gaussian heat maps were utilized based on recently published literature on cardiac landmark localization [65].

For each cardiac view, inputs consisted of 2D images throughout the cardiac cycle. To provide temporal information, the input for each time point t was concatenated with 2D images from t-2, t-1, t+1, and t+2, producing a final 2D + time input with 5 channels. Prior to training, the inputs were resized to 256 x 256 pixels using bicubic interpolation and normalized to have a minimum of 0 and maximum of 1. To improve model generalizability, real-time data augmentations were utilized during training, including random rotations (+/- 10%), random zooms (+/- 20%), random translations (+/- 10%), random contrast adjustments (+/- 15%), the addition of Gaussian noise, and histogram equalizations.

Network Architecture

The anatomical landmark localization networks utilized the U-net architecture, an encoder-decoder with skip connections between mirrored layers in the encoder and decoder stacks [66]. Scaled exponential linear units (SELU) were utilized for activation, with a LeCun normal kernel initializer [67]. An individual U-net network was optimized for each cardiac view, with the number of output channels determined by the number of landmarks present in each

16

view.

Optimization and Evaluation

For each cardiac view, a U-net network was optimized with a mean squared error loss function for a total of 150 epochs using a batch size of 40 and a stochastic gradient descent optimizer with a learning rate of 1e-5 and momentum of 0.9. Following training, performance for each network was assessed using absolute distance errors between predicted and ground truth landmarks. For insertion points, the angulation error between predicted and ground truth valve and septal planes was also measured.

1.3.8   Myocardial Image Segmentation

Dataset and Preprocessing

All 111 cases in the training set and all 12 cases in the validation set were used to optimize the myocardial image segmentation networks. From these cases, the 2CH LT, 2CH RT, 3CH, 4CH, RVOT, and optimal SA slices were selected. Ground truth myocardial image segmentations were generated from contours that were manually drawn at ED and ES for each view by an expert analyst with greater than 10 years of cardiac modeling experience using Segment (Medviso, Lund, Sweden) [68]. The LV papillary muscles and RV trabeculae were included in the blood pool. In the 2CH LT view, the LV cavity and LV myocardium were labeled. In the 2CH RT and RVOT views, the RV cavity and RV myocardium were labeled. In the 3CH, 4CH, and SA views, the LV/RV cavity and LV/RV myocardium were labeled.

For each cardiac view, inputs consisted of 2D images at ED and ES. Prior to training, inputs were cropped to their non-zero regions and normalized to have a minimum of 0 and maximum of 1. To improve model generalizability, real-time data augmentations were utilized during training, including random rotations (+/- 10%), random zooms (+/- 20%), random brightness and contrast adjustments (+/- 15%), the addition of Gaussian noise and blur, gamma correction, mirroring, and the simulation of low resolution.

Network Architecture

The myocardial image segmentation networks utilized the nnU-net architecture, an encoder-decoder with skip connections between mirrored layers in the encoder and decoder stacks [69]. This architecture was chosen based on the results of prior multi-vendor, multi-disease myocardial segmentation challenges [70]. Leaky rectified linear units (ReLU) were utilized for activation [71], with an instance normalization initializer [72]. An individual nnU-net was optimized for each cardiac view, with the number of output channels determined by the number of cavity and myocardium labels present in each view.

Optimization and Evaluation

For each cardiac view, an nnU-net network was optimized with a sum of cross-entropy and Dice loss function [73] for a total of 100 epochs using a batch size of 10 and a stochastic gradient descent optimizer with an initial learning rate of 0.01 and Nesterov momentum of 0.99. The learning rate was decayed throughout training following the 'poly' learning rate policy [74]. Following training, performance for each network was assessed using Dice scores [75] and Hausdorff distances [76] between predicted and ground truth contours using a single fold validation.

Interobserver Analysis

To further characterize the performance of the nnU-net segmentations, an interobserver analysis was conducted to determine the variation in myocardial segmentations between two human observers. In this analysis, two expert analysts, each with greater than 10 years of cardiac modeling experience, manually drew contours of the RV and LV myocardium and blood pool at ED and ES for each cardiac view using Segment (Medviso, Lund, Sweden) [68]. This analysis was performed for a subset of 36 cases from the training and validation sets. Dice scores between contours drawn by the two analysts were calculated and compared to the Dice scores achieved by the nnU-net network.

1.3.9 Automated Cardiac Shape Modeling Pipeline Testing

The automated cardiac shape modeling pipeline was tested by comparing manually and automatically generated shape models from study participants in the test set. Automatically generated models were first aligned with manually generated models using a rigid registration. Euclidean projection distances were then calculated between points on the automatically generated models and surfaces on the manually generated models, which was the metric used to compute the mean absolute error (MAE) in a global and regional error analysis. Global ventricular measurements were also compared between the manually and automatically generated models by computing LV and RV volumes and masses at ED and ES by numerical integration of mesh volumes. Lastly, manually and automatically generated models were projected onto an ED/ES shape atlas constructed from the shape models in the training/validation set and computed Z-scores were compared.

1.3.10 Statistical Analysis

Statistical analysis was carried out using the SciPy Python library (https://www.scipy.org). Summary characteristics of study participants in the training/validation and test sets are reported as mean ± standard deviation or as median (interquartile range), depending on the distribution, for continuous variables and as the count for categorical variables. Normality was tested using Shapiro-Wilks. Differences between these groups were assessed using two-sample t-tests or Wilcoxon rank-sum tests, depending on the distribution, for continuous variables and Pearson's chi-squared tests for categorical variables. The AAFD between predicted and manual labels in the validation set was compared to the AAFD between two manual analyst labels in the validation set using a two-sided t-test. Differences in global ventricular measurements for manually and automatically generated shape models in the test set were assessed using paired-sample t-tests. The distribution of Z-scores for the manually and automatically generated shape models were assessed by a two-sample Kolmogorov-Smirnov test with a significance level of 0.05 and a

Holm-Bonferroni correction for multiple comparisons.

1.4 Results

1.4.1 Individual Network Performance

View Classification

Precision, recall, and F1-scores for view classification predictions on the validation set are shown in Table 1.3. Cardiac views were reliably classified.

Slice Selection

Precision, recall, and F1-scores for slice selection predictions on the validation set are shown in Table 1.4. SA slices were reliably classified.

Phase Selection

The AAFD between predicted ES phase labels and manual labels in the validation set is shown in Table 1.5. The AAFD between two manual analyst labels in the validation set is shown for reference. There was no significant difference between the AAFD between the predicted and manual labels and the AAFD between interobserver labels, as assessed by a two-sided t-test with a significance level of 0.05.

Anatomical Landmark Localization

Absolute distance errors between predicted and ground truth anatomical landmarks in the validation set are shown in Table 1.6. For insertion points, the angulation error between predicted and ground truth valve and septal planes is also shown. Representative anatomical landmark localization predictions are shown in Figure 1.3. Anatomical landmarks were reliably localized.

Myocardial Image Segmentation

Dice scores and Hausdorff distances between predicted and ground truth contours in the validation set are shown in Table 1.7. Representative myocardial image segmentation

predictions are shown in Figure 1.4. Segmentation performance was found to be highly reliable and comparable to the interobserver segmentation error between two expert manual analysts, as shown in Table 1.8.

1.4.2   Automated Cardiac Shape Modeling Pipeline Results

Comparison with Manual Models

A representative output of the cardiac shape modeling pipeline is shown in Figure 1.5, which depicts the myocardial contours and anatomical landmark points that are generated for each cardiac view that are then fit to a subdivision surface template mesh to build a three-dimensional, biventricular shape model. In order to assess the performance of the automated pipeline, the MAE between manually and automatically generated models in the test set was computed. This was done on a global and regional basis for ED and ES models as shown in Table 1.9. The overall error of the automated models is within voxel resolution of the original CMR images for ED models and approximately at voxel resolution for ES models (Table 1.2). In order to assess systematic inward or outward surface displacement of the automated models compared to the manual models, the average algebraic Euclidean projection distance for each coordinate point in the biventricular surface mesh was computed and is shown in Figure 1.6. Global ventricular measurements including volume and mass metrics were also compared between manually and automatically generated models in the test set. A summary of the global ventricular measurements computed in manually and automatically generated models is shown in Table 1.10, along with the differences and correlations. Figure 1.7a shows regression plots and Figure 1.7b shows Bland-Altman plots between global ventricular measurements for manually and automatically generated models.

Pipeline Timing and Manual Intervention Requirements

For a subset of the test set (n=12), the time required to generate cardiac shape models using the automated pipeline was recorded. Statistics were recorded at multiple institutions for

multiple users. Shape models were generated in 5.1 ± 2.8 minutes on average per model (range 2.5 – 10.2 minutes). This represents a significant time savings over manual approaches, which typically take 60-90 minutes on average for a single model. For this subset of cases, the number of times manual override was required was also recorded. The automated pipeline was designed so the user could manually override the automated predictions at each step if necessary. Manual override was only required during the landmark localization step, with interventions occurring for 11.4% of landmarks. The most frequently corrected predictions were for the aortic valve insertions (40% of corrections) and pulmonary valve insertions (40% of corrections). A summary of the necessary manual overrides can be seen in Table 1.11.

Evaluation of Useability for Statistical Shape Modeling

In order to assess the robustness of the automated cardiac shape modeling pipeline for statistical shape modeling applications, the manually and automatically generated models in the test set were projected onto an ED/ES shape atlas derived from shape models in the training/validation set. The mean absolute difference in Z-scores between manually and automatically generated models was then computed for the first 20 modes of the atlas (Figure 1.8), which explain approximately 87% of the shape variation in the training/validation set cases. The mean absolute difference in Z-score was below one standard deviation for each of the first 20 modes, and the average mean absolute difference in Z-score for the first 20 modes was 0.5 standard deviations. The distribution of Z-scores for the manually and automatically generated models were not significantly different for each of the first 20 modes, except mode 8, as assessed by a two-sample Kolmogorov-Smirnov test with a significance level of 0.05 and a Holm-Bonferroni correction for multiple comparisons.

1.5   Discussion

In this study, we demonstrate the use of deep learning for automated view classification, slice selection, phase selection, anatomical landmark localization, and myocardial image seg-

mentation that together provide an end-to-end pipeline for cardiac shape modeling. While others have developed automated cardiac shape modeling pipelines [77, 78, 79, 80], the pipeline presented herein is the first, to our knowledge, to reliably generate three-dimensional, biventricular shape models, including all four valves, from a raw CMR image dataset for the challenging anatomies seen in rTOF. Overall, the automated pipeline performed well on an independent, multi-institutional test set that included a variety of CMR scanners, including several models that were not included in the training/validation set. (Figure 1.2 and Table 1.2).

The highest errors between the automated and manual models were observed around the valve planes (Table 1.9 and Figure 1.6). This was probably due to the high sensitivity of the fitting of the biventricular subdivision surface template mesh to the location of the valve insertion points, which are extremely sparse compared with the contour points used to fit the LV and RV endocardial and epicardial surfaces. Even with manually generated biventricular shape models, slight deviations in the locations of the valve insertion points can result in significant differences in the valvular anatomy of the fitted models.

With this new automated cardiac shape modeling pipeline, which includes a manual confirmation or override for each step of the workflow, a single cardiac shape model can be made in 5.1 ± 2.8 minutes on average, whereas manual models generally require 60-90 minutes per model for an expert analyst. This dramatic reduction in processing time can be useful for estimating global ventricular volumes and masses, for which the automatically generated models demonstrated good agreement with the manual models (Table 1.10 and Figure 1.7). Although differences between automated and manual models reached statistical significance for several global measurements, the magnitude of these differences were small and unlikely to be clinically significant. Moreover, these differences and correlations were similar to previously reported manual interobserver errors and differences between existing clinical techniques, such as the error between cardiac MRI and echocardiography [81, 82]. The reduction in processing time can also significantly increase the throughput and clinical translation of more specific atlas-based analyses of biventricular shape. The automatically generated models were able to capture

23

relevant features of regional ED/ES shape variation to within 0.5 standard deviations on average per mode compared with the manually generated models (Figure 1.8). With this automated workflow, the analysis of large retrospectively collected datasets, such as the INDICATOR cohort [83], can be rapidly achieved, yielding larger and more comprehensive statistical atlases for shape, biomechanics, and electrophysiology analyses with more statistical power when assessing relationships with independent measures of outcome. Additionally, with an end-to-end pipeline that has processing times more consistent with clinical workflows, the ability to deploy atlas-based analyses in a point-of-care clinical setting to quantify patient-specific anatomy, function, or risk relative to the population would be greatly enhanced.

1.5.1   Limitations

In the current iteration of the pipeline, the anatomical landmark localization and my-ocardial image segmentation networks were only trained on cardiac shape models created at ED and ES. This was done because reference manual anatomical landmarks and segmentations for training/validation were only available at ED and ES. This can readily be extended to other timepoints, however, by validating the automated model performance on timepoints throughout the cardiac cycle compared to manual models derived at these same timepoints. Doing so would enable the quantification of dynamic information throughout the cardiac cycle and enable the creation of statistical atlases with much greater temporal resolution. This could assist in the analysis of the effects of ventricular electrophysiologic activation (e.g. bundle branch block, pacing, large scars or patches) on shape and biomechanics. Since the current pipeline was designed as a series of five steps, each of the networks can be improved upon independently of each other. This modularity will be especially useful for extending the automated pipeline to other CHDs with two ventricle morphology, such as coarctation of the aorta, because testing, performance assessment, and any required network retraining will need to be done only on specific steps as needed.

In this study, the ES phase was selected based on the LV cavity in a mid-ventricular SA

slice. For some patients, the presence of right bundle branch blocks or other dyssynchrony may necessitate the selection of independent LV and RV phases. The demonstration of statistical shape modeling presented in this manuscript requires temporal synchronization and the selection of a single ED and ES phase, which may lead to inaccuracies in the RV in the setting of a right bundle branch block. However, the pipeline provides the option of manually selecting independent LV and RV phases, allowing the user to select the option most appropriate for their analyses.

1.6   Conclusions

Through the use of deep learning, we were able to automate all of the major steps involved in constructing three-dimensional, biventricular shape models including view classification, slice selection, phase selection, anatomical landmark localization, and myocardial image segmentation. To our knowledge, this is the first fully automated, end-to-end pipeline that can robustly create shape models for the challenging anatomies present in rTOF. With this approach, we can greatly reduce the manual input required to create shape models enabling the rapid analysis of large-scale datasets and the potential to deploy statistical atlas-based analyses in point-of-care clinical settings.

1.7   Acknowledgments

Chapter 1, in full, is a reprint of the material as it appears in the following article: Govil S*, Crabb BT*, Deng Y, Toso LD, Puyol-Anton E, Pushparajah K, Hegde S, Perry JC, Omens JH, Hsiao A, Young AA, McCulloch AD. A Deep Learning Approach for Fully Automated Cardiac Shape Modeling in Tetralogy of Fallot. *Journal of Cardiovascular Magnetic Resonance*. (2023). The dissertation author is the co-first author of this paper.

Table 1.1. Summary characteristics of study participants in the training/validation and test sets.

Characteristic	Training/Validation Set (n=123)	Test Set (n=30)	p-value
Sex (m/f)	73/50	15/15	0.35
Age (y)	17 (12-26)	22 ± 13	0.47
Height (cm)	161 (150-168)	163 (155-176)	0.07
Weight (kg)	58 ± 25	63 ± 18	0.31
BSA (m^2)	1.57 ± 0.42	1.72 (1.52-1.82)	0.27
LV EDV (mL)	128 ± 44	119 ± 36	0.31
LV ESV (mL)	66 (51-83)	60 (47-70)	0.19
LV SV (mL)	59 ± 21	57 ± 16	0.52
LV EF (%)	48 (41-52)	48 ± 7	0.23
LV Mass (g)	118 ± 35	111 ± 33	0.28
RV EDV (mL)	205 ± 67	197 ± 51	0.54
RV ESV (mL)	127 ± 46	121 ± 37	0.48
RV SV (mL)	78 ± 28	76 ± 23	0.78
RV EF (%)	38 ± 7	39 ± 7	0.72
RV Mass (g)	58 (43-77)	53 ± 24	0.16

Data are reported as mean ± standard deviation or as median (interquartile range), depending on the distribution, for continuous variables and as the count for categorical variables. Normality was tested using Shapiro-Wilks. Differences between the training/validation set and test set were assessed using two-sample t-tests or Wilcoxon rank-sum tests, depending on the distribution, for continuous variables and Pearson's chi-squared tests for categorical variables. BSA: body surface area; LV: left ventricular; RV: right ventricular; EDV: end-diastolic volume; ESV: end-systolic volume; SV: stroke volume; EF: ejection fraction.

Table 1.2. CMR acquisition data for study participants in the training/validation and test sets.

Parameter	Training/Validation Set (n=123)	Test Set (n=30)
Imaging		
Flip Angle (°)	64 (15-80)	57 (45-81)
Phase Spatial Resolution (mm)	1.9 (0.9-3.0)	1.4 (0.5-2.1)
Frequency Spatial Resolution (mm)	1.6 (0.8-2.8)	1.4 (0.5-2.1)
Slice Thickness (mm)	7.1 (4.0-10.0)	7.7 (4.5-10.0)
Repetition Time (ms)	15.8 (2.6-48.7)	16.6 (2.7-60.5)
Echo Time (ms)	1.4 (1.1-3.3)	1.4 (1.1-1.8)
Magnetic Field Strength		
1.5 Tesla	120 (98)	30 (100)
3 Tesla	3 (2)	-
Manufacturer		
Siemens	55 (45)	13 (43)
Philips Medical Systems	41 (33)	8 (27)
GE Medical Systems	27 (22)	9 (30)
Model		
Avanto	55 (45)	3 (10)
Intera	41 (33)	8 (27)
Discovery MR450	14 (11)	3 (10)
Signa HDxt	10 (9)	1 (3)
Discovery MR750w	3 (2)	-
Aera	-	10 (33)
Achieva	-	3 (10)
Ingenia	-	2 (7)

Numerical data are reported as mean (range). Categorical data are reported as the count (percentage). CMR: cardiovascular magnetic resonance.

Table 1.3. Precision, recall, and F1-scores for cardiac view classification predictions on the validation set.

Cardiac View	Precision	Recall	F1-score
2CH LT	0.88	0.94	0.91
2CH RT	0.96	0.95	0.96
3CH	0.38	0.83	0.52
4CH	0.85	0.92	0.89
LVOT	1.00	0.92	0.96
RVOT	0.78	0.79	0.79
SA	0.90	0.96	0.93
OTHER	0.97	0.89	0.93

2CH LT: two-chamber left; 2CH RT: two-chamber right; 3CH: three-chamber; 4CH: four-chamber; LVOT: left ventricular outflow tract; RVOT: right ventricular outflow tract; SA: short axis.

Table 1.4. Precision, recall, and F1-scores for SA slice selection predictions on the validation set.

SA Slice Optimality	Precision	Recall	F1-score
Optimal	0.81	0.93	0.86
Non-optimal	0.96	0.87	0.91

SA: short axis.

Table 1.5. AAFD between predicted ES phase labels and manual labels in the validation set. The AAFD between two manual analyst labels in the validation set is shown for reference.

	Predicted vs. Manual	Interobserver	p-value
AAFD	1.15 ± 1.02	1.39 ± 1.35	0.18

The AAFD is reported as mean ± standard deviation. AAFD: average absolute frame difference; ES: end-systolic.

Table 1.6. Anatomical landmark localization distance errors and valve and septal plane angulation errors in the validation set.

Cardiac View and Anatomical Landmark	Distance Error (mm)	Plane	Angulation Error (°)
3CH View			
MV Insert 1	7.1 ± 3.4	MV	14.3 ± 12.2
MV Insert 2	6.4 ± 3.3		
AV Insert 1	10.8 ± 7.5	AV	19.5 ± 17.0
AV Insert 2	9.8 ± 7.5		
4CH View			
MV Insert 1	4.3 ± 2.6	MV	7.1 ± 5.7
MV Insert 2	6.0 ± 3.3		
TV Insert 1	4.9 ± 2.7	TV	10.2 ± 13.1
TV Insert 2	5.0 ± 3.4		
LV Apex	6.2 ± 3.6		
RVOT View			
PV Insert 1	13.6 ± 8.1	PV	48.7 ± 37.8
PV Insert 2	17.0 ± 10.4		
SA View			
RV Insert 1	5.9 ± 5.3	Septal	8.7 ± 13.5
RV Insert 2	5.0 ± 3.2		

Distance and angulation errors are reported as mean ± standard deviation. 3CH: three-chamber; 4CH: four-chamber; RVOT: right ventricular outflow tract; SA: short axis; LV: left ventricular; RV: right ventricular; MV: mitral valve; AV: aortic valve; TV: tricuspid valve; PV: pulmonary valve.

Table 1.7. Myocardial image segmentation Dice scores and Hausdorff distances in the validation set.

Cardiac View and Contour	Dice Score	Hausdorff Distance (pixels)
2CH LT View		
LV cavity	0.96 ± 0.02	2.73 ± 1.04
LV myocardium	0.88 ± 0.06	2.94 ± 1.13
2CH RT View		
RV cavity	0.97 ± 0.02	3.66 ± 2.40
RV myocardium	0.79 ± 0.12	4.88 ± 3.04
3CH View		
LV cavity	0.96 ± 0.02	3.57 ± 1.68
LV myocardium	0.90 ± 0.03	4.25 ± 3.90
RV cavity	0.95 ± 0.02	2.90 ± 1.95
RV myocardium	0.76 ± 0.09	5.98 ± 6.28
4CH View		
LV cavity	0.97 ± 0.01	2.57 ± 1.34
LV myocardium	0.90 ± 0.03	4.07 ± 3.12
RV cavity	0.96 ± 0.03	3.60 ± 2.73
RV myocardium	0.77 ± 0.12	3.74 ± 2.06
RVOT View		
RV cavity	0.94 ± 0.03	4.05 ± 2.32
RV myocardium	0.78 ± 0.09	4.25 ± 2.48
SA View		
LV cavity	0.94 ± 0.03	4.51 ± 3.05
LV myocardium	0.90 ± 0.02	5.40 ± 3.22
RV cavity	0.94 ± 0.02	4.50 ± 2.35
RV myocardium	0.78 ± 0.03	8.62 ± 3.94

Dices scores and Hausdorff distances are reported as mean ± standard deviation. 2CH LT: two-chamber left; 2CH RT: two-chamber right; 3CH: three-chamber; 4CH: four-chamber; RVOT: right ventricular outflow tract; SA: short axis; LV: left ventricular; RV: right ventricular.

Table 1.8. Interobserver analysis results showing myocardial image segmentation Dice scores between two expert analysts for a subset of the training and validation sets (n=36).

Cardiac View and Contour	Dice Score
LA Views	
LV cavity	0.94 ± 0.05
LV myocardium	0.83 ± 0.06
RV cavity	0.91 ± 0.12
RV myocardium	0.54 ± 0.13
SA View	
LV cavity	0.94 ± 0.08
LV myocardium	0.83 ± 0.07
RV cavity	0.91 ± 0.06
RV myocardium	0.60 ± 0.12

Dices scores are reported as mean ± standard deviation. LA: long axis; SA: short axis; LV: left ventricular; RV: right ventricular.

Table 1.9. MAE between manually and automatically generated shape models in the test set based on projection distance.

MAE (mm)	ED	ES
Global	1.9 ± 0.5	2.1 ± 0.7
Region		
LV Endocardium	1.6 ± 0.7	1.8 ± 1.0
RV Endocardium	1.8 ± 0.5	2.1 ± 0.5
Septum	1.3 ± 0.4	1.4 ± 0.5
Epicardium	2.2 ± 0.8	2.5 ± 1.0
MV	4.6 ± 0.5	5.6 ± 0.7
AV	5.2 ± 0.1	5.4 ± 0.3
TV	3.6 ± 0.6	3.9 ± 0.5
PV	3.1 ± 0.3	3.0 ± 0.3

Numerical data are reported as mean ± standard deviation. MAE: mean absolute error; ED: end-diastole; ES: end-systole; LV: left ventricular; RV: right ventricular; MV: mitral valve; AV: aortic valve; TV: tricuspid valve; PV: pulmonary valve.

Table 1.10. Average global ventricular measurements for manually and automatically generated shape models in the test set as well as differences and correlations.

Measure	Manual Cases	Automated Cases	Difference	R^2	p-value
LV EDV (mL)	119 ± 36	114 ± 37	-5 ± 10 (-4%)	0.93	<0.05
LV ESV (mL)	62 ± 24	64 ± 23	2 ± 9 (3%)	0.85	0.26
LV SV (mL)	57 ± 16	50 ± 18	-7 ± 8 (-12%)	0.82	<0.01
LV EF (%)	48 ± 7	44 ± 7	-5 ± 6 (-9%)	0.45	<0.01
LV Mass (g)	111 ± 33	118 ± 37	8 ± 12 (7%)	0.89	<0.01
RV EDV (mL)	197 ± 51	191 ± 54	-6 ± 17 (-3%)	0.90	0.07
RV ESV (mL)	121 ± 37	114 ± 36	-7 ± 13 (-6%)	0.88	<0.01
RV SV (mL)	76 ± 23	77 ± 29	1 ± 15 (1%)	0.76	0.67
RV EF (%)	39 ± 7	40 ± 10	1 ± 7 (3%)	0.55	0.39
RV Mass (g)	53 ± 24	54 ± 25	0.2 ± 7 (0.4%)	0.93	0.83

Numerical data are reported as mean ± standard deviation. Differences between the manual and automated cases were assessed using paired-sample t-tests. LV: left ventricular; RV: right ventricular; EDV: end-diastolic volume; ESV: end-systolic volume; SV: stroke volume; EF: ejection fraction.

Table 1.11. Occurrence of manual overrides for landmark localization predictions when using the automated pipeline for a subset of the test set (n=6 internal cases, n=6 external cases).

Landmark	Manual Overrides
AV Inserts	16 of 48 (33%)
PV Inserts	16 of 48 (33%)
MV Inserts	8 of 96 (8%)
RV Inserts	0 of 148 (0%)
LV Apex	0 of 12 (0%)
Total	40 of 352 (11.4%)

Occurrences are reported as count (percentage). AV: aortic valve; PV: pulmonary valve; MV: mitral valve; RV: right ventricular; LV left ventricular.
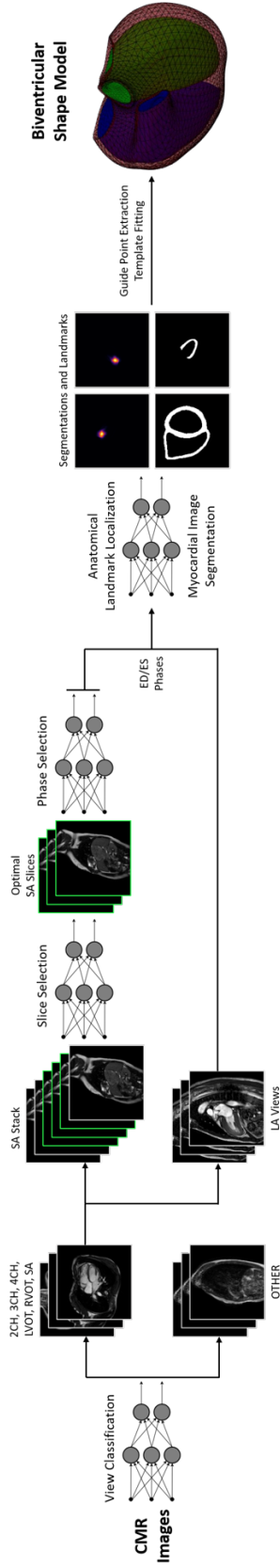
Figure 1.1. Overview of the automated cardiac shape modeling pipeline. The automated pipeline was developed as a series of five steps for view classification, slice selection, phase selection, anatomical landmark localization, and myocardial image segmentation. CMR: cardiovascular magnetic resonance; 2CH: two-chamber; 3CH: three-chamber; 4CH: four-chamber; LVOT: left ventricular outflow tract; RVOT: right ventricular outflow tract; SA: short axis; LA: long axis; ED: end-diastole; ES: end-systole.
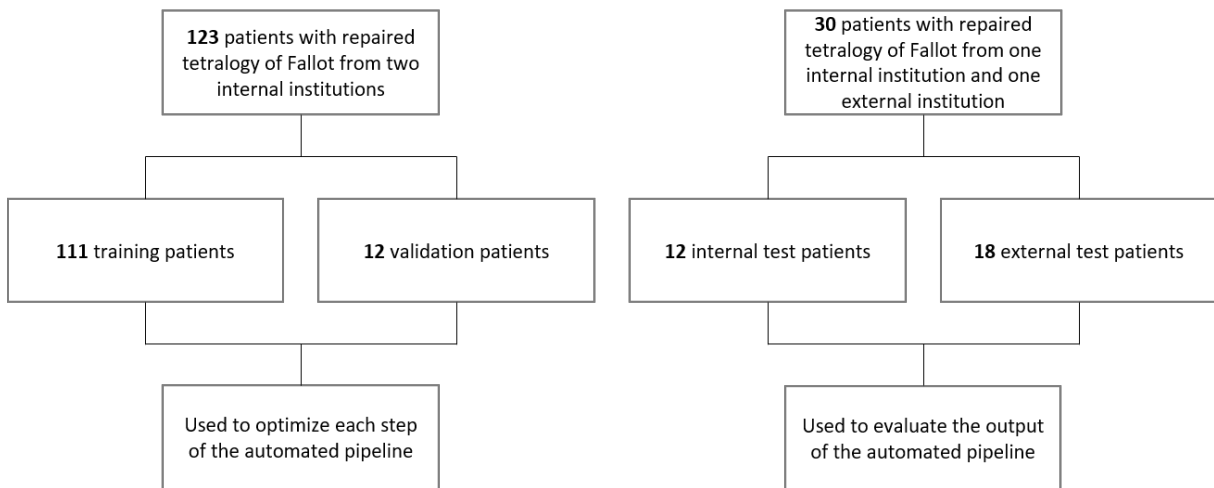
Figure 1.2. Flow-diagram of internal and external datasets used to train, validate, and test the automated cardiac shape modeling pipeline. Cases from the training/validation set were used to optimize each step of the automated pipeline, while cases from the test set were used to evaluate the generalizability of the automated pipeline.
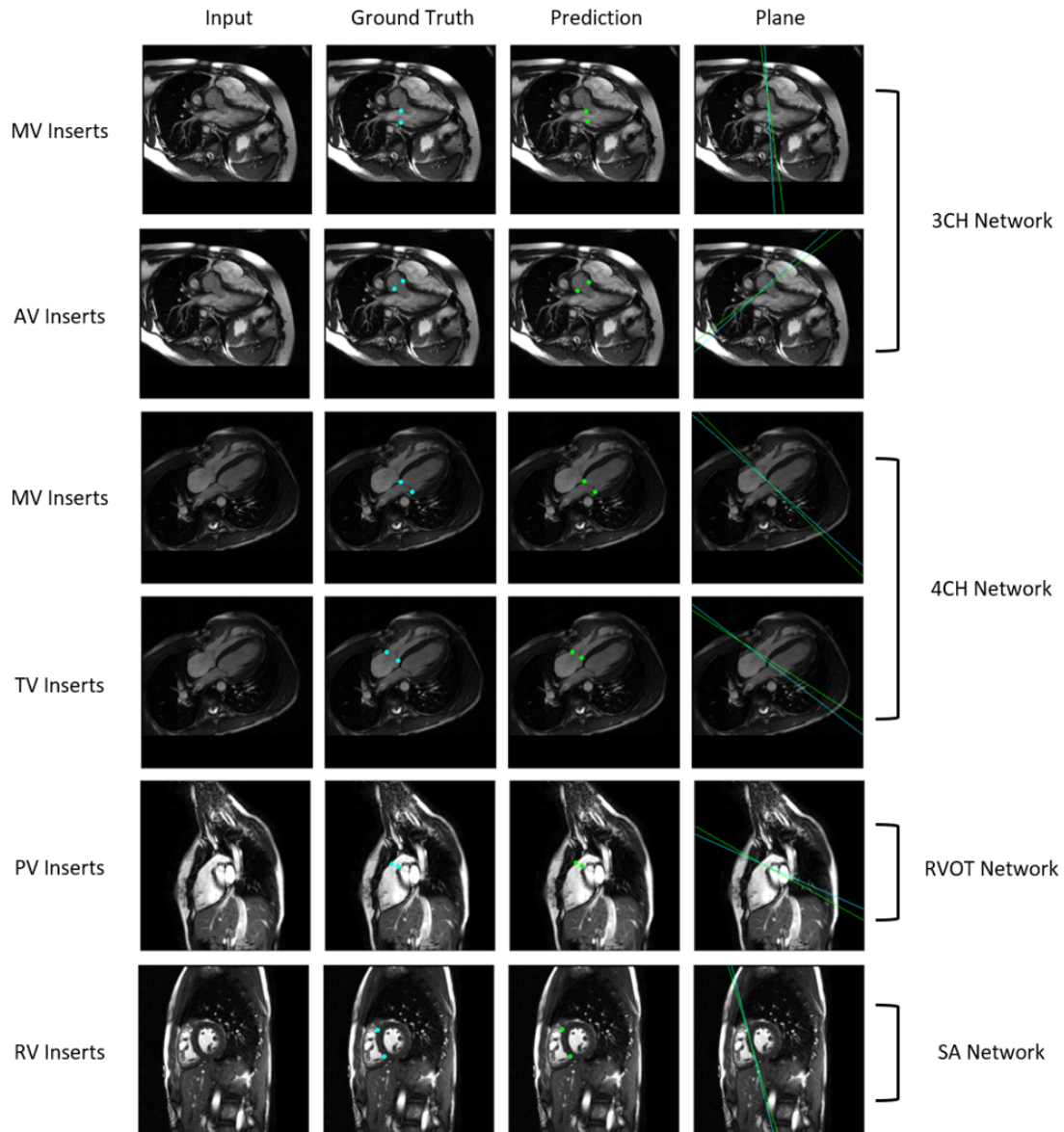
Figure 1.3. Representative anatomical landmark localization predictions for the 3CH, 4CH, RVOT, and SA views. 3CH: three-chamber; 4CH: four-chamber; RVOT: right ventricular outflow tract; SA: short axis; RV: right ventricular; MV: mitral valve; AV: aortic valve; TV: tricuspid valve; PV: pulmonary valve.
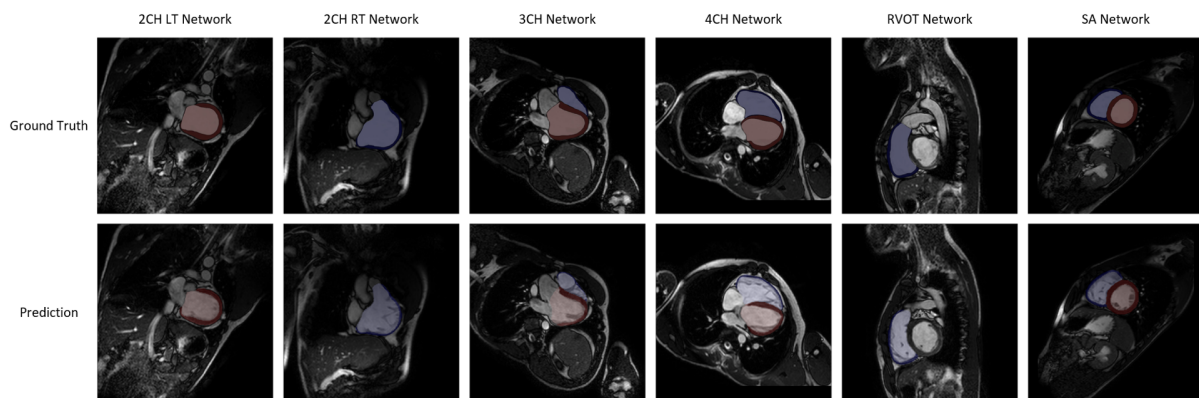
Figure 1.4. Representative myocardial image segmentation predictions for the 2CH LT, 2CH RT, 3CH, 4CH, RVOT and SA views. 2CH LT: two-chamber left; 2CH RT: two-chamber right; 3CH: three-chamber; 4CH: four-chamber; RVOT: right ventricular outflow tract; SA: short axis.
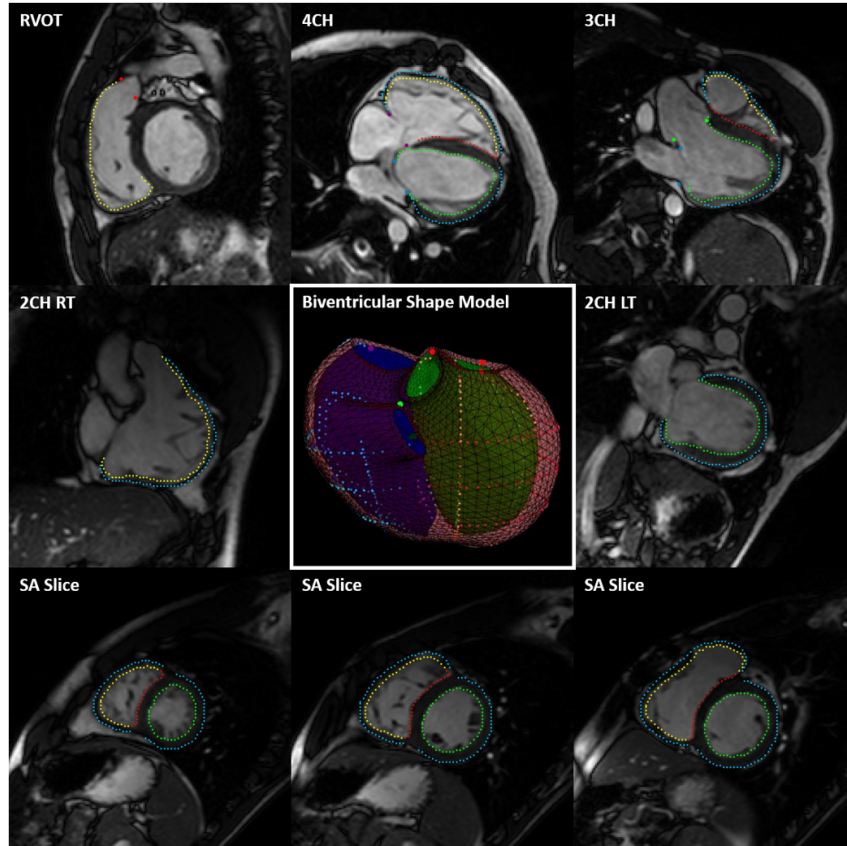
Figure 1.5. Representative output of the automated cardiac shape modeling pipeline. Extracted contour points for the LV endocardium (green), RV endocardium (yellow), epicardium (cyan), and septum (red) and anatomical landmark points for the MV (blue), AV (green), TV (purple), and PV (red) are shown on corresponding views (outside). The contour points and anatomical landmark points were then fit to a biventricular subdivision surface template mesh resulting in a patient-specific biventricular shape model (center) with surfaces for the LV endocardium (green), RV endocardium (blue), and epicardium (maroon). 2CH LT: two-chamber left; 2CH RT: two-chamber right; 3CH: three-chamber; 4CH: four-chamber; RVOT: right ventricular outflow tract; SA: short axis; LV: left ventricular; RV: right ventricular; MV: mitral valve; AV: aortic valve; TV: tricuspid valve; PV: pulmonary valve.
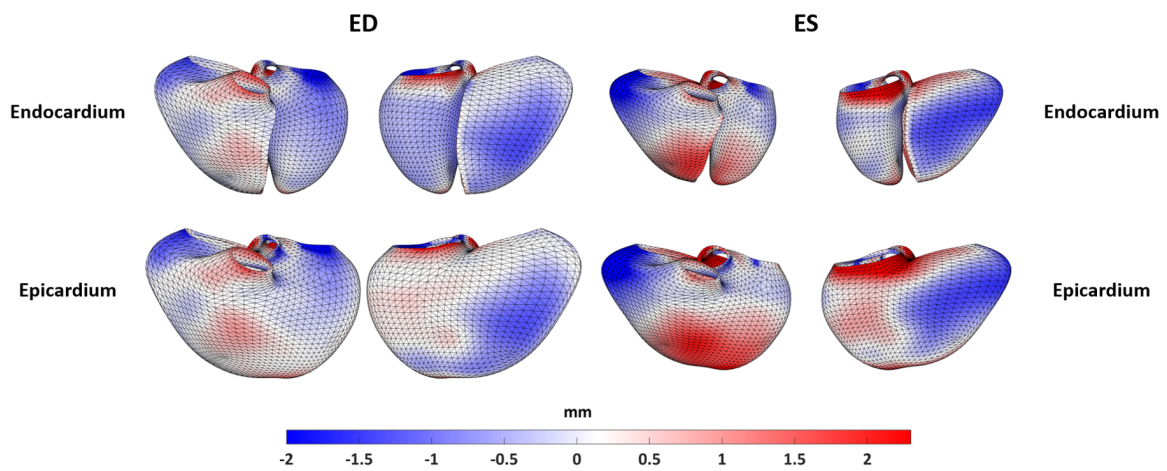
Figure 1.6. Average inward (blue) and outward (red) Euclidian projection distances between manually and automatically generated shape models in the test set. The range of the color bar accounts for 99% of the observed errors. ED: end-diastole; ES: end-systole.
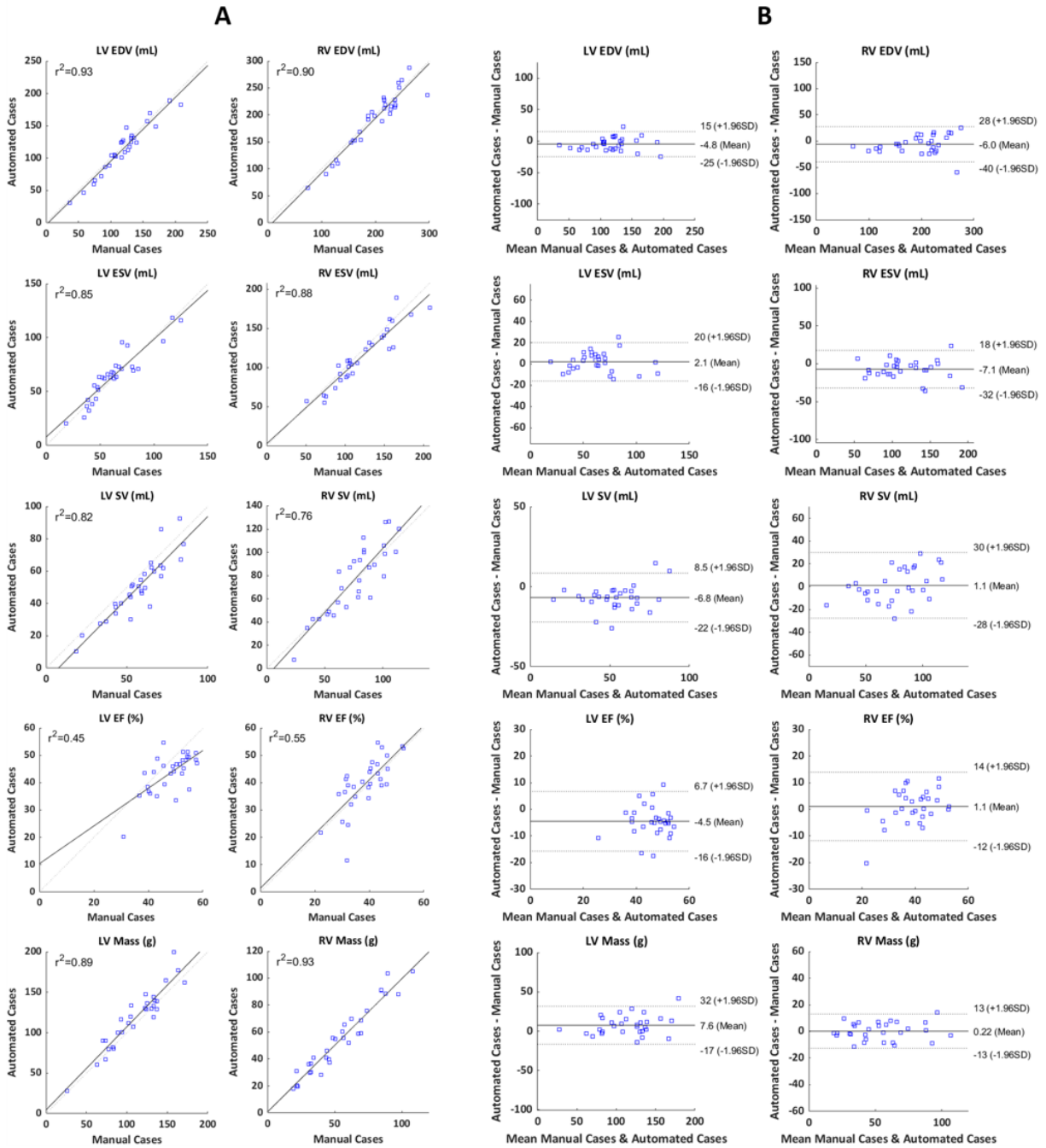
Figure 1.7. A) Regression plots showing the correlation between global ventricular measurements for manually and automatically generated shape models in the test set. **B)** Bland-Altman plots comparing the correlation of global ventricular measurements for manually and automatically generated shape models in the test set. LV: left ventricular; RV: right ventricular; EDV: end-diastolic volume; ESV: end-systolic volume; SV: stroke volume; EF: ejection fraction.
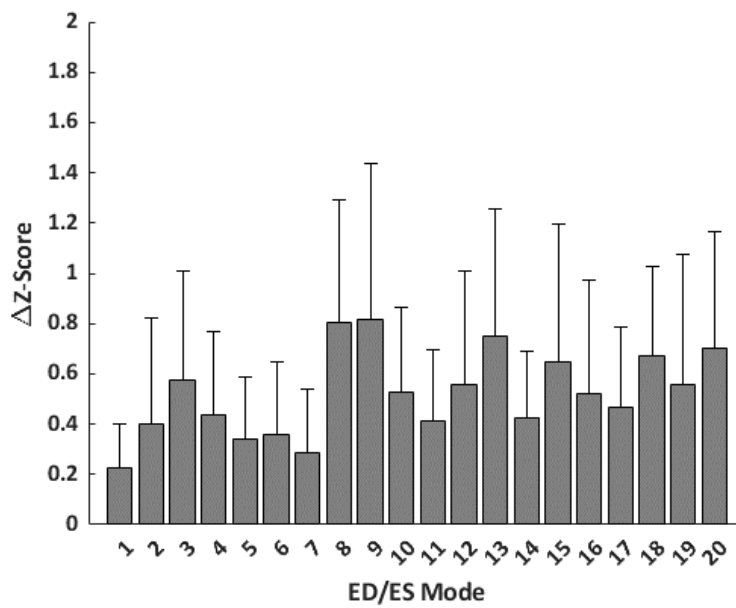
Figure 1.8. Z-score difference between manually and automatically generated shape models in the test set projected onto an ED/ES shape atlas constructed from shape models in the training/validation set. Bars show the average absolute difference in Z-score, and error bars show the standard deviation. ED: end-diastole; ES: end-systole.

Chapter 2

Biventricular Shape Modes Discriminate Pulmonary Valve Replacement in Tetralogy of Fallot Better Than Imaging Indices

2.1 Abstract

Current indications for pulmonary valve replacement (PVR) in repaired tetralogy of Fallot (rTOF) rely on cardiovascular magnetic resonance (CMR) image-based indices but are inconsistently applied, lead to mixed outcomes, and remain debated. This study aimed to test the hypothesis that specific markers of biventricular shape may discriminate differences between rTOF patients who did and did not require subsequent PVR better than standard imaging indices. In this cross-sectional retrospective study, biventricular shape models were customized to CMR images from 84 rTOF patients. A statistical atlas of end-diastolic shape was constructed using principal component analysis. Multivariate regression was used to quantify shape mode and imaging index associations with subsequent intervention status (PVR, n=48 vs. No-PVR, n=36), while accounting for confounders. Clustering analysis was used to test the ability of the most significant shape modes and imaging indices to discriminate PVR status as evaluated by a Matthews correlation coefficient (MCC). Geometric strain analysis was also conducted to assess shape mode associations with systolic function. PVR status correlated significantly with shape modes associated with right ventricular (RV) apical dilation and left ventricular (LV)

dilation (p<0.01), RV basal bulging and LV conicity (p<0.05), and pulmonary valve dilation (p<0.01). PVR status also correlated significantly with RV ejection fraction (p<0.05) and correlated marginally with LV end-systolic volume index (p<0.07). Shape modes discriminated subsequent PVR better than standard imaging indices (MCC=0.49 and MCC=0.28, respectively) and were significantly associated with RV and LV radial systolic strain. Biventricular shape modes discriminated differences between patients who did and did not require subsequent PVR better than standard imaging indices in current use. These regional features of cardiac morphology may provide insight into adaptive vs. maladaptive types of structural remodeling and point toward an improved quantitative, patient-specific assessment tool for clinical use.

2.2 Background

Tetralogy of Fallot (TOF) is the most common cyanotic congenital heart disease (CHD) accounting for about 7-10% of all congenital cardiac malformations [1]. Current twenty-five-year mortality rates are $\leq 5\%$, but long-term sequelae in adult survivors with repaired tetralogy of Fallot (rTOF) lead to an acceleration in mortality thereafter [18]. Common late consequences of repair include residual pulmonary regurgitation (PR) and chronic right ventricular (RV) volume overload, which in turn are associated with exercise intolerance, arrhythmia, RV and/or left ventricular (LV) dysfunction, and a higher risk of sudden cardiac death [84, 85]. The main strategy for preserving RV function relies on timely surgical or transcatheter pulmonary valve replacement (PVR), which has been shown to alleviate symptoms, normalize RV volumes, and improve RV function [86, 87]. However, there continues to be disparity in the indications and timing for PVR [88, 89, 90], which must strike a balance between being performed early enough to prevent irreversible adverse remodeling but late enough to reduce the number of re-interventions and potential surgical complications [29].

Current indications for PVR rely on cardiovascular magnetic resonance (CMR) imaging, which is the gold standard for evaluation of RV volumes, severity of PR, and RV function [37, 38].

The American College of Cardiology / American Heart Association, the Canadian Cardiovascular Society, and the European Society of Cardiology provide recommendations on indications for performing PVR [32, 31, 30]; though, they are largely qualitative in nature, recommending intervention in cases of moderate to severe RV dysfunction and/or moderate to severe RV enlargement. Quantitative indications for intervention are based on global measures of cardiac mass and volume [91, 92], e.g. RV end-diastolic volume index (EDVi) >160mL/m^2 and/or RV end-systolic volume index (ESVi) >80ml/m^2, but these thresholds are subject to institutional bias and lead to mixed outcomes, leaving the subject up for debate [93]. While these indications have been guided by several CMR-based imaging studies, the wealth of morphological and functional information available in CMR images has been under-utilized, not taking into account three-dimensional, regional analysis of geometry and function.

Several studies have shown that bulging of the RV outflow tract, dilation of the RV apex, dilation of the pulmonary valve annulus, and a more circular tricuspid valve are associated with adverse remodeling in rTOF, specifically in the presence of chronic PR [94, 95]. Other studies of RV remodeling in rTOF have shown that a decrease in RV free wall curvature is associated with a decrease in regional RV function as measured by a lower area strain [96]. However, these prognostic markers are not captured by global measures of ventricular function or used in current clinical decision-making to indicate intervention.

The current study employed a statistical atlas-based approach to condense morphological data from CMR imaging into quantitative, interpretable markers of regional biventricular shape. These atlas-based biomarkers were assessed in their ability to discriminate differences in shape between patients who required subsequent PVR and those who did not, and the performance of these novel biomarkers was compared with standard imaging indices. The aim was to discover specific markers of cardiac morphology that could discriminate differences in adverse remodeling within the rTOF population, regarding referral for subsequent PVR, better than standard imaging indices.

2.3 Methods

2.3.1 Study Population

CMR images and associated clinical data from 84 rTOF patients were obtained retrospectively from the Cardiac Atlas Project (CAP) database [59]. The CAP is a worldwide consortium that facilitates clinical data sharing and development of computational methods for analysis of cardiac structure and function across several CHD cohorts (https://www.cardiacatlas.org). Deidentified datasets employed in this study were contributed from two clinical centers (Rady Children's Hospital, San Diego, CA, US and The Center for Advanced Magnetic Resonance Imaging, Auckland, NZ) with approval from local institutional review boards via waiver of informed consent (UCSD IRB 201138 and HDEC 16/STH/248, respectively). Patients were divided into two groups, one in which patients were referred for PVR following imaging (PVR, n=48) and one in which patients were not referred for PVR following imaging (No-PVR, n=36), within a four-year period. Patients with previous PVR were excluded from the study. Patients with significant tricuspid regurgitation or only mild pulmonary insufficiency (PR fraction <20%) by CMR were also excluded, such that the patients included in the study demonstrated an RV volume overload phenotype due strictly to moderate to severe PR. Out of the forty-eight patients included in the PVR cohort, twenty-six of them were symptomatic. The most common symptoms were tiredness, shortness of breath, and exercise intolerance, and in some cases, symptoms included chest pain or palpitations. While essentially all rTOF patients have a right bundle branch block (RBBB) pattern, none of the subjects in this study had significant degrees of atrial or ventricular ectopy or atrioventricular conduction disturbance. The decision to perform PVR at Rady Children's Hospital was largely based on the criteria outlined by Tal Geva [93], which includes thresholds for RV EDVi, RV ESVi, and RV and LV ejection fraction (EF), where the number of criteria that need to be met are reduced if the subject is symptomatic. The decision to perform PVR at The Center for Advanced Magnetic Resonance Imaging was based on the same threshold for RV EDVi as the Tal Geva criteria [93], significantly reduced RV and LV EF, and

considerations for the presence of symptoms. Summary characteristics of the study participants grouped by PVR status are shown in Table 2.1. Study participants from The Center for Advanced Magnetic Resonance Imaging were on average ten years older and included proportionally more female subjects than study participants from Rady Children's Hospital. Participants from each of these centers were unequally represented in each clinical group contributing to significant differences in age and sex between these groups. Quantitative data regarding the degree of pulmonary valve stenosis were available for study participants from Rady Children's Hospital San Diego. In this cohort, 90% of the patients demonstrated mild pulmonary valve stenosis as defined by a pulmonary valve peak gradient of less than 36 mmHg on an echo six months within the CMR exam date. In addition, based on clinical notes, none of the study participants from The Center for Advanced Magnetic Resonance Imaging had severe pulmonary valve stenosis.

2.3.2   CMR Image Acquisition and Analysis

Each patient underwent functional CMR examination within the scope of standard clinical practice. CMR images were acquired using 1.5T MRI scanners, including Siemens Avanto (Siemens Medical Systems) and GE Discovery (GE Healthcare Systems). Two-dimensional cine images were acquired using steady-state free procession imaging and were prospectively or retrospectively gated during breath-hold. Short-axis slices were obtained parallel to the tricuspid annulus plane, spanning both ventricles from apex to base. Long-axis slices were obtained through all valve annuli in standard 4-chamber, 2-chamber, LV outflow tract, and RV outflow tract views. Typical imaging parameters included: repetition time 24-32ms; echo time 1.1-1.5ms; flip angle 70-80°; field of view 200-300mm x 200-300mm; spatial resolution 0.59-1.75mm × 0.59-1.75mm x 4-6mm; and number of time frames 20-35.

Contours were drawn manually at end-diastole (ED) and end-systole (ES) on both short-axis and long-axis cine slices using Segment (Medviso). Papillary muscles were excluded from the endocardial contour segmentation. Mitral and tricuspid valve landmark points were defined from the intersection of the left and right atrial and ventricular contours delineated on the

4-chamber and 2-chamber long-axis images. Aortic valve landmark points were defined from the LV outflow tract images, and pulmonary valve landmark points were defined from the RV outflow tract images. When aortic and pulmonary leaflets were not visible, boundary points were defined by the change in appearance of the myocardial and vessel wall.

Antegrade and retrograde pulmonary flow measurements were obtained from two-dimensional phase-contrast (PC) imaging using commercially available software, including Argus Flow (Siemens Healthineers) and cvi42 (Circle Cardiovascular Imaging). PC analysis of antegrade and retrograde flows in the main artery was performed on a plane just below the pulmonary artery bifurcation and perpendicular to the axis of the pulmonary artery. Typical imaging parameters included: repetition time 4.8-5.0ms; echo time 2.3-3.0ms; flip angle 15-30°; field of view 169-315mm x 300-420mm; spatial resolution 1.4-2.0mm x 1.4-2.0mm x 5-8mm; temporal resolution 37-41ms; and acceleration factor 3. Scouts were used to set the velocity encoding.

CMR image analysis was performed by a senior researcher with more than ten years of cardiac image analysis experience. The expert analyst was blinded regarding the patient's PVR status.

2.3.3 Biventricular Shape Analysis

A biventricular subdivision surface template mesh was constructed including the LV endocardium, RV endocardium, epicardium, and all four valves as described previously [61]. The template mesh was automatically customized to each patient while correcting for breath-hold slice misregistration using an iterative registration algorithm. Valve locations were customized to the manual landmark points via landmark registration, and surfaces were customized to the manual contours via diffeomorphic non-rigid registration. Standard imaging indices, including LV and RV volumes and masses at ED and ES, were calculated by numerical integration of mesh volumes, which has previously shown good agreement with slice summation of manual contours [61, 47].

To build a biventricular atlas of ED shape, patient-specific ED surface points were first aligned to population mean ED surface points by a rigid registration. Following the alignment, principal component analysis (PCA) was used to evaluate the distribution of shape variation across the rTOF cohort. PCA is an unsupervised dimensional reduction technique that, in this case, condenses cardiac shape features into statistical Z-scores represented as orthogonal components (modes), ranked by the amount of shape variance they explain in the population, that quantify degrees of patient-specific shape difference from the population mean.

2.3.4 Shape Mode Subset Selection

A subset of biventricular shape modes was chosen from the rTOF atlas to create a feature set with the same number of variables as standard imaging indices calculated (10 variables). Modes that cumulatively explained greater than 95% of the variation in shape in the rTOF cohort were ranked for predicting PVR status using chi-square tests, which is a commonly used technique for univariate feature ranking for classification. The 10 modes with the highest predictive importance score were retained for multivariate associations with PVR status.

2.3.5 Multivariate Associations with PVR Status

Multivariate regression models were constructed to quantify imaging index and biventricular shape associations with PVR status, while accounting for confounders. Sex, type of repair, time after repair, and body surface area (BSA) were included in the models to control for differences that exist in these characteristics between the PVR and No-PVR cohorts. When testing associations with imaging indices, the response variable was each imaging index. In these models, PVR status, sex, and type of repair were included as categorical predictors, and time after repair was included as a continuous predictor. When testing associations with biventricular shape, the response variable was the morphometric score for each shape mode. In these models, PVR status, sex, and type of repair were included as categorical predictors, and time after repair and BSA were included as continuous predictors. Imaging indices and shape modes that had the

51

most significant associations with PVR status after accounting for confounders were retained for clustering to discriminate PVR status.

2.3.6   Clustering Analysis to Discriminate PVR Status

K-means clustering, an unsupervised clustering method, was employed to characterize the discriminatory power of imaging indices and biventricular shape (minimum two variables required in each feature set). Patients were divided into two clusters using the cosine distance metric to ignore the absolute sizes of measurements and only consider their relative sizes. The ability of imaging indices and shape modes to discriminate the PVR and No-PVR cohorts in these clusters was assessed through a matching matrix. The Matthews correlation coefficient (MCC) was used to measure the quality of clinical classification, which has been shown to be more reliable than accuracy and F1 score [97].

2.3.7   Geometric Strain Analysis

Geometric strain analysis was conducted to assess if differences in imaging indices and biventricular shape that are associated with PVR status are also associated with differences in systolic function. Longitudinal strain (LS), circumferential strain (CS), and radial strain (RS), which represent longitudinal shortening, shortening along the circular perimeter, and thickening of the wall, respectively, were calculated from geometric arc length changes between ED and ES using the Cauchy strain formula and have shown good agreement with myocardial strains calculated from myocardial tagging [98, 99]. LS and CS were calculated from the model mesh, and RS was calculated using a modified version of the centerline method [100] using the intersection between short-axis slices and the model mesh. The interventricular septum was included in the calculation for LV systolic strain. Univariate regression models were applied to quantify the association between LV and RV systolic strains and imaging indices and shape modes associated with PVR status.

2.3.8   Statistical Analysis

Statistical analysis was carried out using the SciPy Python library (https://www.scipy.org). Summary characteristics for the two groups are reported as mean ± standard deviation or as median (interquartile range), depending on the distribution, for continuous variables and as frequency for categorical variables. Normality was tested using Shapiro-Wilks. Differences between the two groups were tested using unpaired two-sample t-tests or Wilcoxon rank-sum tests, depending on the distribution, for continuous variables and Pearson's chi-squared tests for categorical variables. All variables were normalized before regression and k-means clustering. Statistical associations in the regression analyses are denoted by p-values with a significance level of 0.05.

2.4   Results

2.4.1   Standard Imaging Index Features

Models were successfully customized to manual contours and landmark points for all patients. Ventricular volumes and masses were calculated by numerical integration of mesh volumes, and PR volumes were calculated from PC imaging. Together these measurements constituted the feature set of standard imaging indices used in subsequent analyses. Measurements were indexed to BSA. Summary imaging indices for the PVR and No-PVR cohorts are shown in Table 2.2.

2.4.2   Biventricular Shape Features

PCA on anatomically co-registered models of 84 rTOF patient hearts yielded a statistical shape atlas comprised of 83 orthogonal components (modes). The percent of shape variance explained by each mode and cumulatively for the first 35 modes is shown in Figure 2.1a. The first 30 modes explained greater than 95% of the shape variation in the population and were ranked for predicting PVR using chi-square tests. PVR status predictor ranks and importance

scores for the first 30 modes are shown in Figure 2.1b. The 10 modes with the highest predictive importance score are labeled and constituted the set of biventricular shape features used in subsequent analyses, equal to the number of standard imaging indices calculated.

2.4.3 Imaging Indices and Shape Modes Associated with PVR Status

Multivariate regression models were constructed to quantify imaging index and biventricular shape associations with PVR status while accounting for confounders including sex, type of repair, time after repair, and BSA. Summary results of imaging index and shape mode associations with PVR status are shown in Table 2.3.

In the feature set of standard imaging indices, RV EF was significantly associated with PVR status, in which patients in the PVR cohort had lower RV EF than patients in the No-PVR cohort (Table 2.2). LV ESVi was the next most highly associated with PVR status, in which patients in the PVR cohort had higher LV ESVi than patients in the No-PVR cohort (Table 2.2). RV EF and LV ESVi were retained for clustering analysis from the imaging index feature set to meet the minimum two variables required.

In the set of biventricular shape features, three shape modes were significantly associated with PVR status: ED4, ED6, and ED25. Shape changes along each of these modes are shown in Figure 2.2 in addition to Z-scores for the PVR and No-PVR cohorts. ED4 appears to be a specific marker of opposing RV apical dilation and LV dilation; ED6 appears to be a specific marker of RV basal bulging and LV conicity; and ED25 appears to be a specific marker of pulmonary valve dilation. Patients in the PVR cohort demonstrated increased RV basal bulging, LV dilation, LV conicity, and pulmonary valve dilation, while patients in the No-PVR cohort demonstrated increased RV apical dilation. ED4, ED6, and ED25 were retained for clustering analysis from the shape mode feature set.

2.4.4 Performance of Imaging Indices and Shape Modes in Discriminating PVR Status

K-means clustering was employed to assess the ability of imaging indices and biventricular shape to discriminate between patients in the PVR and No-PVR cohorts. The results of the clustering analysis for each subset of features are shown in Figure 2.3a. The number of patients in the PVR and No-PVR cohorts in each cluster for each subset of features are shown in Figure 2.3b. From these results, a matching matrix was constructed and the MCC was calculated to assess the performance of clinical classification for each subset of features as shown in Figure 2.3c, in which the predicted class was taken to be the dominant cohort in each cluster. The subset of shape modes discriminated patients in the PVR and No-PVR cohorts with much greater performance than the subset of standard imaging indices (MCC=0.49 and MCC=0.28, respectively).

2.4.5 Imaging Indices and Shape Modes Associated with Geometric Strain

Geometric strain analysis was used to assess if differences in imaging indices and biventricular shape that are associated with PVR status are also associated with differences in systolic function. Summary systolic strains for the PVR and No-PVR cohorts are shown in Figure 2.4a. RV and LV RS were highly significantly associated with PVR status after accounting for confounders. For imaging indices, univariate regression analysis revelated that RV EF was highly significantly associated with LV LS, RV LS, LV CS, and RV CS ($p<0.0001$) and significantly associated with LV RS ($p<0.05$), where increased RV EF was associated with increased systolic strains. For shape modes, univariate regression analysis revealed that ED4 was highly significantly associated with RV RS as shown in Figure 2.4b. ED6 and ED25 were also significantly associated with RV RS and LV RS, respectively ($p<0.05$). A more positive ED6 and ED25 Z-score was associated with increased RV RS and decreased LV RS, respectively, and vice versa.

2.5 Discussion

Adverse RV remodeling in rTOF has been well juxtaposed with RV morphology in reference healthy populations [101, 102, 103]; differences in RV remodeling within the rTOF population and how they determine referral for subsequent PVR, however, are not well characterized. In this cross-sectional retrospective study, an atlas-based biventricular shape analysis framework was used to quantify specific, regional shape differences associated with PVR status and compared with standard imaging indices in their ability to discriminate patients who did and did not undergo PVR.

2.5.1 Standard Imaging Index Features

Current guidelines [91, 92, 93] recommend PVR in rTOF if progressive RV dilation results in RV EDVi >160mL/m^2 and/or RV ESVi >80mL/m^2; however, significant associations between these indices and subsequent PVR were not found. Interestingly, the degree of PR was also not significantly associated with PVR status, suggesting that the presence of volume overload alone was more important than current assessment of severity. This agrees with studies showing a compensatory increase in RV RS in response to PR and RV volume overload [104, 105]. RV EF and LV ESVi had the highest associations with PVR status, although RV EF was the only imaging index with significant associations with PVR status. This was not unexpected as diminishing RV EF usually accompanies fairly rapid PVR (within a few weeks). These imaging indices were identified as preoperative risk factors for adverse outcomes post-PVR in the INDICATOR cohort study [33, 106], suggesting that these indices are not only associated with subsequent PVR but also are important determinants of long-term outcome.

2.5.2 Biventricular Shape Features

Through biventricular shape analysis and geometric strain analysis, the present study shows that patients in the PVR cohort demonstrated increased RV basal bulging and pulmonary

valve dilation, which was associated with reduced RV and LV RS, while patients in the No-PVR cohort demonstrated increased RV apical dilation, which was associated with increased RV RS. These specific, regional features of shape all contribute to RV dilation, but are not distinguished when relying solely on global ventricular measurements alone. While these shape changes agree with previously characterized features of adverse remodeling in the rTOF population as a whole [94, 95, 96], this study suggests that RV basal bulging may be a form of maladaptive remodeling that leads to RV dysfunction (as in the PVR cohort), while RV apical dilation may be a form of adaptive remodeling that preserves RV function (as in the No-PVR cohort). Several studies have proposed mechanisms by which RV basal bulging may lead to RV dysfunction. One study found that increased RV basal bulging correlated with increased RV vorticity and that these changes in flow could induce abnormal fibrosis in these regions [49]. Another study found that RV basal bulging correlated with increased diastolic force parameters that resulted in decreased RV function [107]. Patients in the PVR cohort also demonstrated increased LV dilation and conicity, which have independently been shown to lead to LV dysfunction in patients with acute myocardial infarction [108]. This is also an important long-term follow-up issue for rTOF patients [109, 110].

By clustering analysis, biventricular shape modes discriminated PVR status better than standard imaging indices, despite the fact that these indices are currently the cornerstone of clinical evaluation for PVR. The clustering analysis was also repeated with the same imaging index and biventricular shape features with only patients that were asymptomatic (Figure 2.5). The performance of the biventricular shape features in discriminating PVR status improved slightly (MCC=0.51), while the performance of the imaging indices in discriminating PVR status decreased (MCC=0.22). A matching matrix was also constructed where the predicted class was taken to be patients that did or did not meet criteria for PVR based on a single standard to avoid institutional bias regarding the decision to perform PVR and the actual class was taken to be whether or not the patient underwent PVR (Figure 2.6). In this case, the set of criteria outlined by Tal Geva [93] was employed, while specifically only accounting for RV

EDVi, RV ESVi, and RV and LV EF thresholds and the presence of symptoms. The overall performance of these criteria in discriminating patients in the PVR and No-PVR cohorts was lower than biventricular shape features (MCC=0.23). Upon closer inspection, these criteria were highly sensitive in discriminating referral for PVR (sensitivity=0.94) but not very specific (specificity=0.22), while biventricular shape features were not as sensitive in discriminating referral for PVR (sensitivity=0.69) but much more specific (specificity=0.81).

2.5.3 Study Limitations

Owing to the retrospective nature of this study, the clinical data available were heterogenous and limited in clinical indicators such as exercise capacity, rhythm disturbances, and functional scores. In the future, prospective studies should be conducted to assess biventricular shape mode relationships with differences in objective measures of outcome before and after PVR, rather than the decision to perform PVR itself, and supervised machine learning methods, such as decision trees or support vector machines, should be employed to fine-tune thresholds for atlas-based biomarkers that can serve as indications for PVR and give the desired specificity or sensitivity to maximize patient benefit. Another limitation of this study was the use of cross-sectional data. The temporal evolution of biventricular shape markers should be evaluated in longitudinal studies to get a better understanding of the time history of ventricular remodeling and how this relates to optimal timing of PVR. Finally, data employed in the study were contributed from multiple centers leading to selection bias that was unequally represented in each group. While confounders were accounted for, future analyses would benefit from an age and sex-matched comparison conducted at a single center.

2.6 Conclusions

Specific biventricular shape modes in rTOF were able to discriminate differences between patients who did and did not require subsequent PVR better than standard imaging indices. These shape modes quantify regional features of cardiac morphology that may provide insight into

adaptive vs. maladaptive types of structural remodeling that may be overlooked when relying solely on standard imaging indices alone. Routine clinical assessment of patients with rTOF using an atlas-based analysis of shape and function may reveal adverse effects of pathophysiologies over time, reduce qualitative observer and institutional measurement biases, and improve timing of interventions and patient prognosis.

2.7   Acknowledgments

Chapter 2, in full, is a reprint of the material as it appears in the following article: Govil S*, Mauger CA*, Hegde S, Occleshaw CJ, Yu X, Perry JC, Young AA, Omens JH, McCulloch AD. Biventricular Shape Modes Discriminate Pulmonary Valve Replacement in Tetralogy of Fallot Better Than Imaging Indices. *Scientific Reports*. (2023). The dissertation author is the co-first author of this paper.

Table 2.1. Summary characteristics grouped by PVR status.

Characteristic	PVR (n=48)	No-PVR (n=36)	p-value
Sex (m/f)	35/13	17/19	0.016
Type of Repair:			0.003
Transannular Patch	35	30	
Valve-Sparing	2	6	
Conduit	11	0	
Age at Repair (y)	0.3 (0.3-0.8)	1 (1-4)	<0.001
Age at CMR (y)	12 (9-16)	20 (16-33)	<0.001
Age at PVR (y)	14 (11-17)	-	
Time After Repair to CMR (y)	12 (9-16)	19 (15-26)	<0.001
Time After CMR to PVR (y)	0.9 (0.3-1.8)	-	
Height (cm)	156 (135-165)	163 (157-167)	0.006
Weight (kg)	49±23	62±18	0.008
BSA (m^2)	1.4±0.4	1.7±0.3	0.002

Normally distributed data are reported as mean ± standard deviation or as median (interquartile range) otherwise.
BSA: body surface area; CMR: cardiovascular magnetic resonance; PVR: pulmonary valve replacement.

Table 2.2. Summary imaging indices grouped by PVR status.

Imaging Index	PVR (n=48)	No-PVR (n=36)	p-value
LV EDVi (mL/m^2)	79±15	79±15	0.923
LV ESVi (mL/m^2)	43±9	41±10	0.341
LV EF (%)	46±6	48±6	0.057
LV Mi (g/m^2)	75±11	72±14	0.341
RV EDVi (mL/m^2)	140±22	138±32	0.723
RV ESVi (mL/m^2)	87±17	80±23	0.110
RV EF (%)	37±6	42±7	0.001
RV Mi (g/m^2)	42±9	39±7	0.080
PRVi (mL/m^2)	27±12	30±17	0.363
PRF (%)	41±10	40±11	0.611

Data are reported as mean ± standard deviation. EDVi: end-diastolic volume index; EF: ejection fraction; ESVi: end-systolic volume index; LV: left ventricular; Mi: mass index; PRF: pulmonary regurgitant fraction; PRVi: pulmonary regurgitant volume index; RV: right ventricular.

Table 2.3. Summary results for imaging index and shape mode associations with PVR status after accounting for sex, type of repair, time after repair, and BSA.

Imaging Index	p-value	Shape Mode	p-value
RV EF	0.043	ED4	0.002
LV ESVi	0.065	ED25	0.003
RV Mi	0.065	ED6	0.022
PRVi	0.113	ED20	0.115
LV EF	0.155	ED3	0.281
LV EDVi	0.226	ED19	0.337
LV Mi	0.376	ED8	0.593
RV ESVi	0.497	ED13	0.594
RV EDVi	0.667	ED11	0.695
PRF	0.837	ED12	0.704

Features in bold have significant associations with PVR status and were retained for clustering analysis. *LV ESVi was also retained for clustering analysis to meet the minimum two variables required for the imaging index feature set. EDVi: end-diastolic volume index; EF: ejection fraction; ESVi: end-systolic volume index; LV: left ventricular; Mi: mass index; PRF: pulmonary regurgitant fraction; PRVi: pulmonary regurgitant volume index; RV: right ventricular.
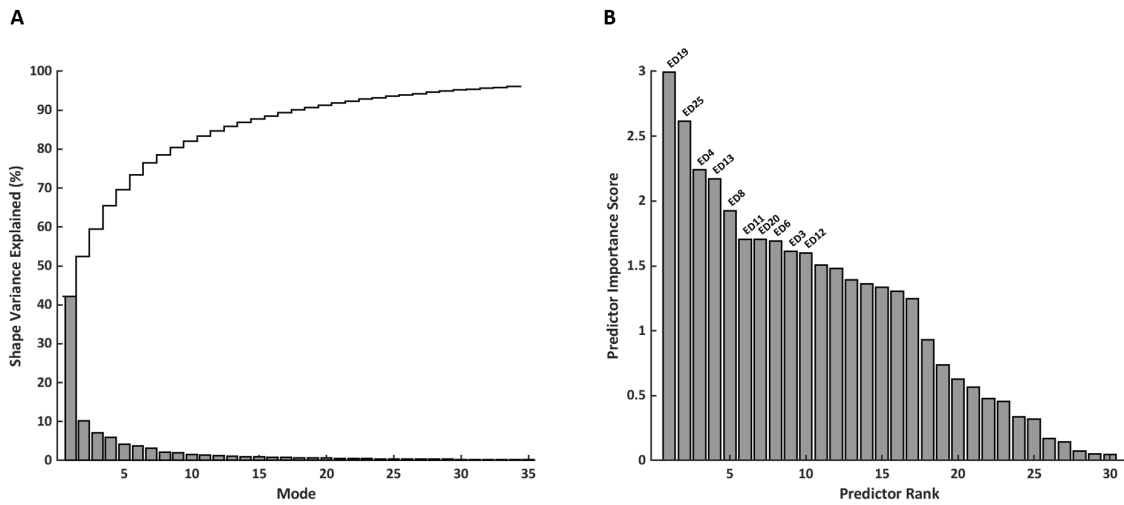
Figure 2.1. Shape mode subset selection from the rTOF atlas. **A)** Shape variance explained (%) per mode (shaded bars) and cumulatively (solid line). **B)** PVR status predictor rank and importance score for modes that explained greater than 95% of shape variation in the population. Labeled shape modes were retained for multivariate associations with PVR status.
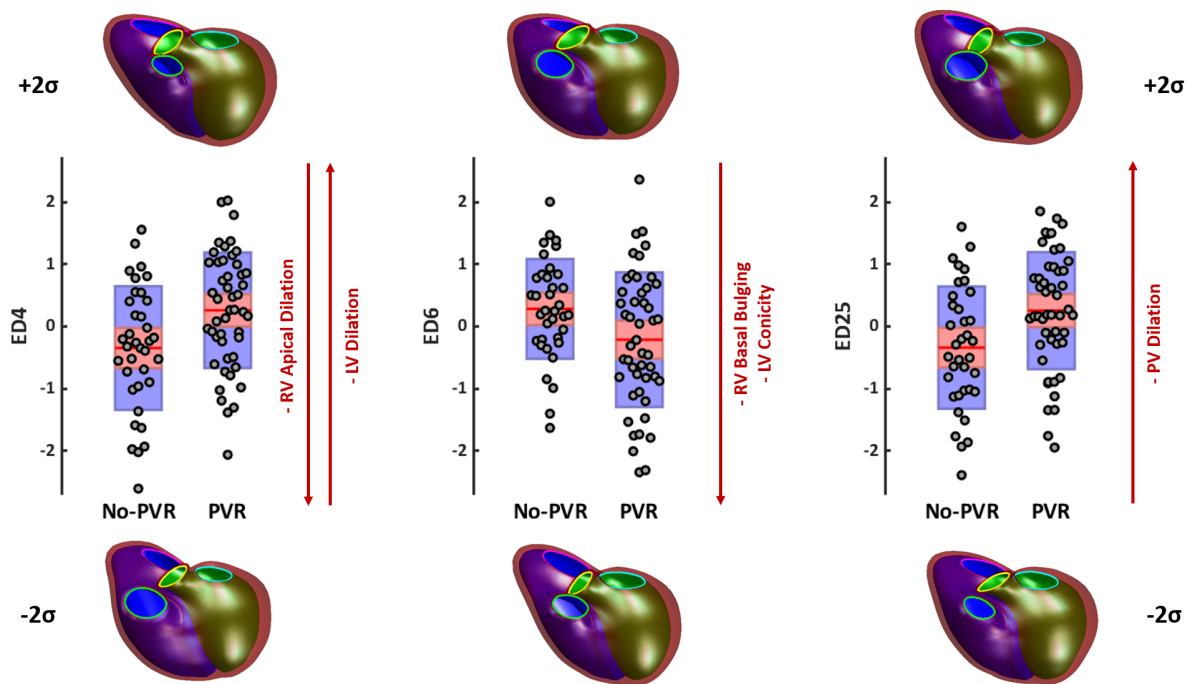
Figure 2.2. Shape modes that have significant associations with PVR status. Box plots show mean (red line), 95% confidence intervals of the mean (pink shaded bar), and one standard deviation of the mean (blue shaded bar) for Z-scores (gray circles). Models show mean ED shape plus two standard deviations (top) and minus two standard deviations (bottom) for each mode. The LV endocardial surface, RV endocardial surface, and epicardial surface are shown in green, purple, and maroon, respectively. The mitral, tricuspid, aortic, and pulmonary valves are shown in cyan, pink, yellow, and green, respectively. LV: left ventricular; PV: pulmonary valve; RV: right ventricular.

Figure 2.3. Summary clustering results depicting the ability of imaging indices (top) and shape modes (bottom) to discriminate PVR status. **A)** K-means clustering using features with the most significant associations with PVR status with two clusters (blue squares: cluster 1; red triangles: cluster 2; filled: PVR; open: No-PVR). **B)** Number of patients in the PVR (dark gray bars) and No-PVR (light gray bars) cohorts in each cluster. **C)** Matching matrix and MCC performance metric for classifying patients by PVR status. EF: ejection fraction; ESVi: end-systolic volume index; LV: left ventricular; MCC: Matthews correlation coefficient; RV: right ventricular.
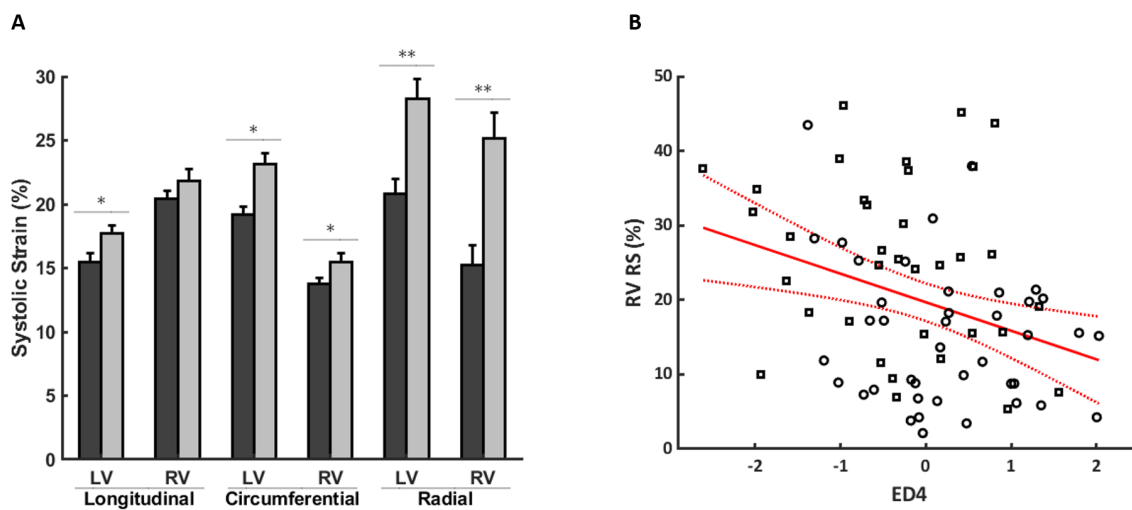
Figure 2.4. Geometric strain analysis. **A)** Summary systolic strains (%) grouped by PVR status (PVR: dark gray bars; No-PVR: light gray bars). Data are reported as mean ± standard error. Systolic CS and LS are conventionally negative, but their absolute values are shown for simpler interpretation. Systolic strains that have significant associations with PVR status after accounting for sex, type of repair, time after repair, and BSA are denoted with symbols (*p<0.05; **p<0.01). **B)** Univariate regression model between RV RS (%) and ED4 (black circles: PVR; black squares: No-PVR; red solid line: linear fit; red dotted lines: 95% confidence bounds; p<0.01; r=0.33). LV: left ventricular; RS: radial strain; RV: right ventricular.
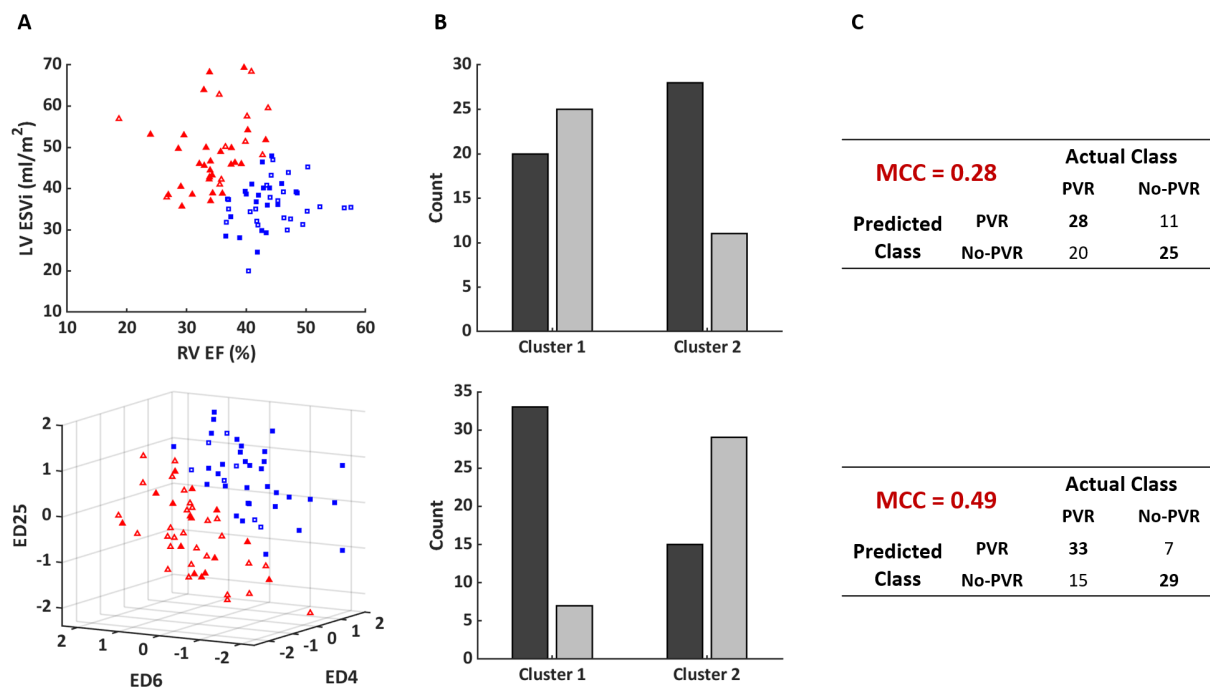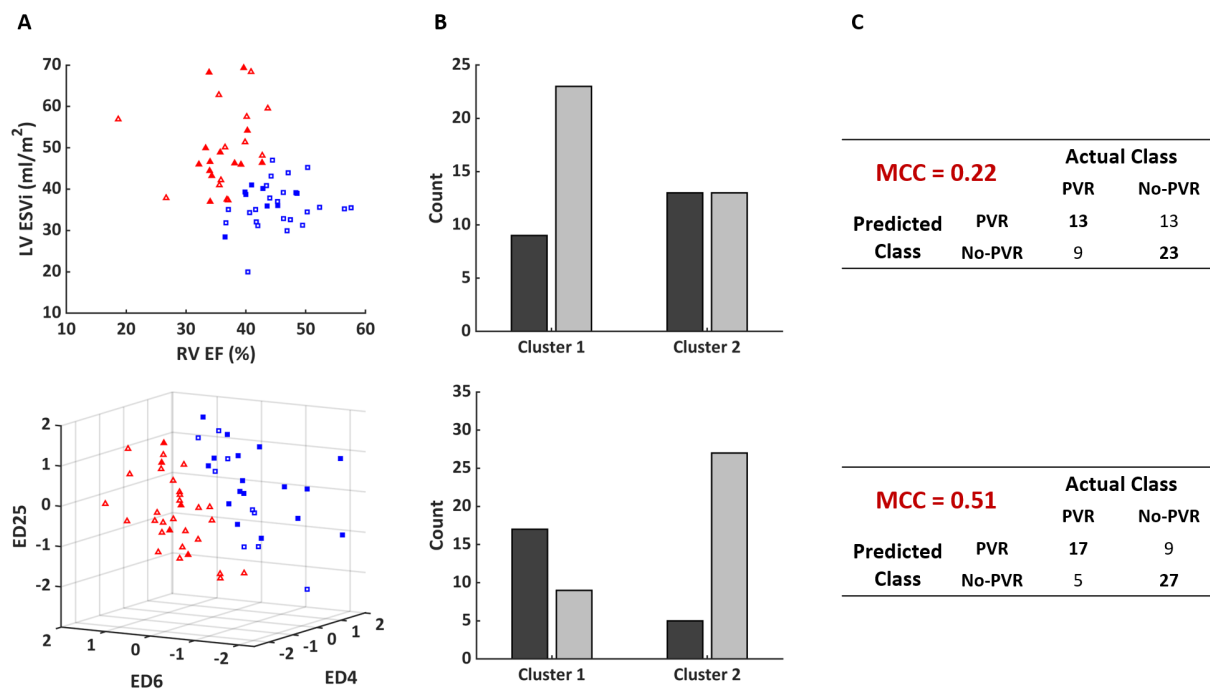
Figure 2.5. Summary clustering results depicting the ability of imaging indices (top) and shape modes (bottom) to discriminate PVR status for asymptomatic patients. **A)** K-means clustering using features with the most significant associations with PVR status with two clusters (blue squares: cluster 1; red triangles: cluster 2; filled: PVR; open: No-PVR). **B)** Number of patients in the PVR (dark gray bars) and No-PVR (light gray bars) cohorts in each cluster. **C)** Matching matrix and MCC performance metric for classifying patients by PVR status. EF: ejection fraction; ESVi: end-systolic volume index; LV: left ventricular; MCC: Matthews correlation coefficient; RV: right ventricular.

	MCC = 0.23	**Actual Class**	
		PVR	**No-PVR**
Predicted	**PVR**	**45**	28
Class	**No-PVR**	3	**8**

Figure 2.6. Matching matrix and MCC performance metric for classifying patients by PVR status based on volume and functional criteria outlined by Tal Geva.

Chapter 3

An Atlas-Based Analysis of Biventricular Mechanics in Tetralogy of Fallot

3.1 Abstract

The current study proposes an efficient strategy for exploiting the statistical power of cardiac atlases to investigate whether clinically significant variations in ventricular shape are sufficient to explain corresponding differences in ventricular wall motion directly, or if they are indirect markers of altered myocardial mechanical properties. This study was conducted in a cohort of patients with repaired tetralogy of Fallot (rTOF) that face long-term right ventricular (RV) and/or left ventricular (LV) dysfunction as a consequence of adverse remodeling. Features of biventricular end-diastolic (ED) shape associated with RV apical dilation, LV dilation, RV basal bulging, and LV conicity correlated with components of systolic wall motion (SWM) that contribute most to differences in global systolic function. A finite element analysis of systolic biventricular mechanics was employed to assess the effect of perturbations in these ED shape modes on corresponding components of SWM. Perturbations to ED shape modes and myocardial contractility explained observed variation in SWM to varying degrees. In some cases, shape markers were partial determinants of systolic function and, in other cases, they were indirect markers for altered myocardial mechanical properties. Patients with rTOF may benefit from an atlas-based analysis of biventricular mechanics to improve prognosis and gain mechanistic insight into underlying myocardial pathophysiology.

3.2 Background

While shape, wall motion, and hemodynamics are important indicators of regional ventricular wall mechanics, they form an incomplete picture. Regional stresses and strains are more direct and sensitive indicators of regional myocardial mechanics because they are related via intrinsic myocardial material properties, such as active myofiber contractility and passive stiffness [111, 112, 113]. Several groups have demonstrated the feasibility of patient-specific biomechanical modeling [114, 115], though this depends on accurate measures of myocardial anatomy, hemodynamics, activation patterns, and wall motion to identify unknown mechanical properties, and still requires material assumptions that cannot be measured in vivo. Patient-specific models of biomechanics are also highly nonlinear, and consequently, their solutions can significantly amplify measurement uncertainties.

The use of statistical shape modeling to characterize major features of ventricular shape and wall motion at the population-level has been insightful for better understanding many cardiac pathologies including several congenital heart diseases. By identifying major modes of variation in biventricular shape and wall motion in various patient cohorts, many groups have observed statistically significant relationships between ventricular shape modes and ventricular function or clinical outcomes [39, 41, 44, 61, 47]. These analyses, however, do not establish causal relationships between shape and function or outcomes. When statistical shape models are integrated with cardiac biomechanics models, however, mechanistic relationships between observable features of cardiac shape, function, and intrinsic myocardial mechanical properties can be tested further, which may be important for understanding and predicting ventricular remodeling. This is particularly relevant in patients with repaired tetralogy of Fallot (rTOF) that face long-term, adverse right ventricular (RV) and/or left ventricular (LV) remodeling as a consequence of surgical repair [37, 110, 33, 116].

The current study proposes an efficient strategy for exploiting the statistical power of cardiac atlases to investigate the extent to which clinically significant variations in ventricular

shape explain corresponding differences in ventricular function directly or whether they are indirect markers of altered myocardial mechanical properties. Patient-specific relationships between end-diastolic shape and systolic wall motion were assessed for consistency with properties representative of the cohort mean and, in the case of deviations, were explored for their ability to explain differences in clinical outcomes. Specifically, in a rTOF patient cohort, we tested the hypothesis that shape variations can be direct determinants of variations in systolic function, but may also be indirect markers of altered myocardial mechanical properties that could help stratify clinical outcomes in rTOF.

3.3 Methods

3.3.1 Study Population and Geometry Fitting

A previously identified cohort of 84 rTOF patients was employed in this study [52]. Cardiovascular magnetic resonance (CMR) images and associated clinical data for this cohort were retrospectively collected from the Cardiac Atlas Project database (https://www.cardiacatlas.org) [59]. Deidentified datasets were contributed from two clinical centers (Rady Children's Hospital, San Diego, CA, US and The Center for Advanced Magnetic Resonance Imaging, Auckland, NZ) with approval from local institutional review boards via waiver of informed consent (UCSD IRB 201138 and HDEC 16/STH/248, respectively). All patients underwent standard-of-care CMR examination, and CMR images were acquired using 1.5T MRI scanners, including Siemens Avanto (Siemens Medical Systems) and GE Discovery (GE Healthcare Systems), as described previously [52]. Three-dimensional, patient-specific geometric models were customized to a biventricular subdivision surface template mesh using manually drawn contours at end-diastole (ED) and end-systole (ES) in Segment (Medviso) along with manually annotated anatomical landmarks, as described previously [52].

3.3.2   Atlas-Based Analysis of Systolic Wall Motion

A statistical atlas of systolic wall motion (SWM) was generated from the patient-specific geometric models at ED and ES. Patient-specific surface points at ED and ES were first aligned to population mean ED surface points by a rigid registration using a Procrustes alignment. A vector field of SWM was then computed between ED and ES for each patient. Principal component analysis (PCA) was then used to evaluate the distribution of SWM across the rTOF cohort.

3.3.3   Sensitivity of Biventricular Function to Systolic Wall Motion

The effects of the first ten SWM modes on LV and RV function were analyzed by varying individual modes and computing corresponding LV and RV ejection fractions (EFs). For each SWM mode, wall motion displacements were calculated for Z-scores between -2 and 2 in steps of 0.5 and were added to the mean ED shape of the rTOF cohort to yield an ES shape. The mean ED model volumes and computed ES model volumes were used to calculate EFs for each score along each mode. The sensitivity of changes in LV and RV EF to changes along an individual SWM mode was then computed using linear regression.

3.3.4   Association of End-Diastolic Shape with Systolic Wall Motion

Associations between ED shape modes and SWM modes were assessed via univariate regression analysis. ED shape modes were taken from an ED shape atlas previously derived from the same cohort of rTOF patients [52]. ED shape modes that were previously found to be significantly associated with differences in prognosis were correlated with the five SWM modes that had the greatest effect on combined LV/RV function. ED shape modes that had significant correlations with systolic wall motion modes were perturbed in a finite element (FE) mechanics framework to assess the degree to which shape markers are direct determinants of systolic function.

3.3.5 Finite Element Analysis of Biventricular Biomechanics

Biomechanics simulations were performed using biventricular, cubic-Hermite FE meshes generated from the ED shape atlas. A compressible, nonlinearly elastic, transversely isotropic constitutive model was used to define the passive material properties of the myocardium in the fiber direction (a, a_f, b, b_f) [117, 118]. Mesh fiber directions were assigned using a rule-based approximation, where fibers were defined relative to the circumferential direction in the LV and RV epicardium as -60° and -25°, respectively, and in the LV and RV endocardium as 60° and 0°, respectively [119]. In order to define a physiologically realistic transmural gradient, fiber directions were linearly interpolated from epicardium to endocardium. Active contraction of the myocardium was governed by a transversely isotropic active tension model, where the transverse direction active force was specified to be 70% of the fiber direction active force. An unloaded, stress-free reference geometry for each simulation was approximated using a previously described iterative, inflation-deflation algorithm [119], with convergence criteria defined as a change in computed ED volumes between successive iterations of less than 2%. Pressure boundary conditions were applied normal to the endocardial surfaces using average LV and RV ED and ES catheterization pressures from rTOF patients with available clinical data. The average LV and RV EDPs were 1.05 kPa and 0.95 kPa, respectively, and the average LV and RV ESPs were 11 kPa and 5.15 kPa, respectively. Additionally, nodal boundary conditions were implemented to constrain epicardial longitudinal and circumferential dis-placement at the valve planes.

Mean passive material properties were approximated by estimating the reference geometry for the mean ED shape. Material constants, b and b_f, were taken from previously reported values from human subjects with heart failure [115], while material constants, a and a_f, were estimated by altering these parameters until the FE-computed ED model volumes at mean ED pressure matched the atlas mean ED model volumes. The material anisotropy ratio of a to a_f was maintained so that only a single parameter was estimated. Mean active material properties were

approximated by linearly increasing the active tension developed in the myocardium until the FE-computed ES model volumes at mean ES pressure matched the atlas mean ES model volumes. These mean passive and active material properties were then used in additional FE simulations with perturbations of ED geometry corresponding to Z-scores of ±2 for tested ED shape modes. The computed ED and ES mesh geometries for each shape perturbation were sampled on the endocardial and epicardial surfaces in order to compute wall motion displacements, which were then projected onto the SWM atlas to compute Z-scores for corresponding SWM modes of interest. SWM mode Z-scores from FE-computed models were compared with those predicted from linear regression models fit to patient data. All FE analysis was performed in Continuity 6 (https://www.continuity.ucsd.edu), a problem-solving environment for multiscale biomechanics and electrophysiology.

3.3.6 Statistical Analysis

Statistical analysis was carried out using the SciPy Python library (https://www.scipy.org). Statistical associations in the regression analysis are denoted by p-values with a significance level of 0.05. A Bonferroni correction was used to adjust the significance level to correct for multiple comparisons.

3.4 Results

3.4.1 Atlas of Systolic Wall Motion and Associations with End-Diastolic Shape

An atlas of SWM was constructed from a cohort of 84 rTOF patients. The first ten SWM modes explained approximately 70% of the variation in the study population (Figure 3.1a), and their effects on LV and RV function were analyzed (Figure 3.1b). ED shape modes that were previously found to be significantly associated with differences in prognosis in rTOF correlated with SWM modes that had the greatest effect on combined LV/RV function (Figure 3.1c).

ED4, which is a specific marker of opposing RV apical dilation and LV dilation, was

significantly correlated with SWM7, which appears to be a specific marker of displacement around the RV base, RV apex, and the entire LV free wall (Figure 3.2a). ED6, which is a specific marker of RV basal bulging and LV conicity, was significantly correlated with SWM8, which appears to be a specific marker of displacement around the posterior RV base, LV base, and LV apex (Figure 3.2b). These ED shape modes were perturbed in a FE model to assess the degree to which shape differences are direct determinants of observed changes in SWM.

3.4.2   Finite Element Analysis of Biventricular Biomechanics

Parameterization of the material properties of the mean FE-computed model resulted in an average absolute error compared with the mean atlas model of 1.06 mm and 1.44 mm at ED and ES, respectively, both of which are within voxel resolution of the original CMR images used to make the patient-specific geometric models (0.6-1.75 mm). The estimated mean passive material properties are shown in Table 3.1, where the approximated stiffness of the RV was twice that of the LV. The mean peak active tension developed in the myocardium was estimated to be 164 kPa in both the LV and RV. A summary of global volume and functional measurements for the mean FE-computed model and atlas model are shown in Table 3.2. Overall, the FE-computed model measurements demonstrate good agreement with the atlas model measurements. Lastly, the resulting SWM Z-scores for the mean FE-computed model were compared to those for the mean atlas model, which are zero by definition, for the first five SWM modes (Figure 3.3). Overall, the Z-score differences between the FE-computed model and atlas model are within an acceptable range.

FE simulations with perturbed ED shapes were executed with mean material properties, and their deformed ES shapes were computed (Figure 3.4). The FE-computed change in LV and RV EF were -5.3% and -0.2%, respectively, along the shape change in ED4 and 3.2% and 3.1%, respectively, along the shape change in ED6. The predicted change in LV and RV EF, based on the correlations between ED shape and SWM and the observed effect on EF (Figure 3.1), were -2.8% and -3.0%, respectively along the shape change in ED4 and -3.4% and -2.0%, respectively,

along the shape change in ED6.

The SWM Z-scores for the FE-computed ED shape perturbations were computed and compared with those predicted from linear regression models fit to patient data. For the correlation between ED4 and SWM7 (Figure 3.5a), the FE-computed slope was -0.12 compared to -0.32 in the patient data. For the correlation between ED6 and SWM8 (Figure 3.5b), the FE-computed slope was 0.02 compared to -0.29 in the patient data. For FE-computed models that did not match the predicted SWM, the model contractility was adjusted to produce a better match. For both ED4 and ED6, a more negative Z-score was associated with increased contractility (Figure 3.6a and Figure 3.6b, respectively).

3.5 Discussion

Patients with rTOF are at risk of developing RV and LV dysfunction as a consequence of adverse ventricular remodeling. While statistical shape modeling has been used to identify features of ventricular remodeling that are associated with function in the rTOF population, it was not clear whether shape features are direct determinants of systolic function. In this study, cardiac biomechanics models were integrated with statistical shape models to test whether clinically significant variations in ventricular shape explain corresponding differences in systolic function or if they are indirect markers of altered myocardial mechanical properties, or both.

3.5.1 Shape Determinants of Biventricular Function

By correlation analysis, previously identified biventricular ED shape modes that had significant associations with differences in prognosis of patients with rTOF were also significantly correlated with the components of SWM that contributed most to differences in LV and RV EF. Specifically, greater RV apical dilation and less LV dilation were associated with greater systolic displacements near the RV base and apex and the entire LV free wall, and greater RV basal bulging and higher LV conicity were associated with greater systolic displacements around the posterior RV base and the LV base and apex. The mechanisms of these shape-function

relationships were tested using FE models in which observed shape mode differences were simulated without changes in material properties or boundary conditions.

In the case of RV apical dilation and LV dilation, differences in the shape alone partially explained observed differences in systolic function. In terms of global functional metrics, less RV apical dilation and greater LV dilation accounted for more than the expected decrease in LV EF (-5.3% vs. -2.8%) but none of the expected decrease in RV EF (-0.2% vs. -3.0%). In terms of regional measures of SWM, differences in the shape alone explained 38% of the variation in wall motion. Assuming that the remaining correlation could be explained by differences in myocardial material properties, we observed that greater RV apical dilation and less LV dilation were associated with increased contractility. Therefore, greater RV apical dilation may be a surrogate for increased RV basal and apical contractility that may also serve as a compensatory mechanism to prevent LV dilation and preserve LV function. This mechanism may explain why patients with rTOF that had greater RV apical dilation and less LV dilation tended to have better prognoses [52].

In the case of RV basal bulging and LV conicity, differences in shape alone explained the opposite change in systolic function. In terms of global functional metrics, less RV basal bulging and lower LV conicity led to an increase in LV and RV EF (3.2% and 3.1%, respectively) rather than an expected decrease in LV and RV EF (-3.4% and -2.0%, respectively). In terms of regional measures of SWM, changing shape alone produced a slope that was the opposite sign as that of the regression model. When altering myocardial contractility to better match the ED shape and SWM relationship, greater RV basal bulging and higher LV conicity were associated with increased contractility. In order to address this discrepancy, RV basal bulging and LV conicity shape mode scores were correlated with patient-specific LV and RV EFs, providing insight into how these shape changes effect overall differences in global function rather than changes in global function along a specific component of SWM. Through this analysis, less RV basal bulging and lower LV conicity were correlated with higher LV and RV EF. Overall, these results suggest that while RV basal bulging and LV conicity may be surrogate measures

for increased contractility in the RV posterior base and LV apex and base, the gain of function in these regions is overshadowed by the loss of function in other regions associated with shape itself. This mechanism may explain why patients with rTOF that had less RV basal bulging and lower LV conicity had better outcomes [52].

3.5.2 Limitations

There were several simplifications that were employed in our FE analysis of biventricular mechanics. Material properties were assumed to be homogeneous throughout different regions of the heart including the entire RV and the entire LV, rather than including more specific regional heterogeneities that could be the result of scarring or fibrosis in areas with surgical incisions. The myocardial fiber architecture employed was also simplified using a rule-based approximation with a linear transmural gradient rather than using more realistic properties. This was primarily due to the lack of information on ventricular fiber architecture in a representative rTOF patient. Differences in hemodynamics between patients that might have also contributed to variation in shape and SWM were not considered due to the limited clinical availability of this data. Lastly, the FE models employed did not include boundary conditions representative of interactions with the pericardium, atria, and great vessels or include fluid-structure interactions.

3.6 Conclusions

In this study, statistical shape models were integrated with cardiac biomechanics models to further investigate the degree to which clinically significant shape markers are determinants of systolic function in a cohort of patients with rTOF. In FE simulations of systolic mechanics, variations in ED shape explained differences in SWM to varying degrees. Variation in RV apical dilation and LV dilation partially explained differences in SWM, while variation in RV basal bulging and LV conicity explained the opposite change in SWM. Specifically, greater RV apical dilation and less LV dilation were associated with increased RV basal and apical contractility and may be important determinants of improved function in rTOF. Overall, patients with rTOF

may benefit from an atlas-based analysis of biventricular mechanics that can provide insight into mechanisms of pathophysiology and aid long-term clinical management.

3.7   Acknowledgments

Chapter 3, in full, is a reprint of the material as it appears in the following article: Govil S, Hegde S, Perry JC, Omens JH, McCulloch AD. An Atlas-Based Analysis of Biventricular Mechanics in Tetralogy of Fallot. *STACOM 2022 International Workshop on Statistical Atlases and Computational Models of the Heart*. (2022). The dissertation author is the first author of this paper.

Table 3.1. Estimated mean passive material properties for finite element computed model.

Region	a (kPa)	a_f (kPa)	b (–)	b_f (–)
LV	1.197	0.8925	9.726	15.779
RV	2.394	1.785	9.726	15.779
Base	11.97	8.925	9.726	15.779

LV: left ventricular; RV: right ventricular.

Table 3.2. Comparison of mean FE-computed model and atlas model volumes and EFs.

Measure	Atlas Model	FE-Computed Model
LV EDV (mL)	78.3	77.9
LV ESV (mL)	38.8	39.7
RV EDV (mL)	153.4	153.3
RV ESV (mL)	89.2	87.9
LV EF (%)	50.5	49.0
RV EF (%)	41.9	42.7

LV: left ventricular; RV: right ventricular; EDV: end-diastolic volume; ESV: end-systolic volume; EF: ejection fraction.

A)

SWM Mode	1	2	3	4	5	6	7	8	9	10
Variance Explained (%)	15	14	10	7	5	4	4	4	3	2
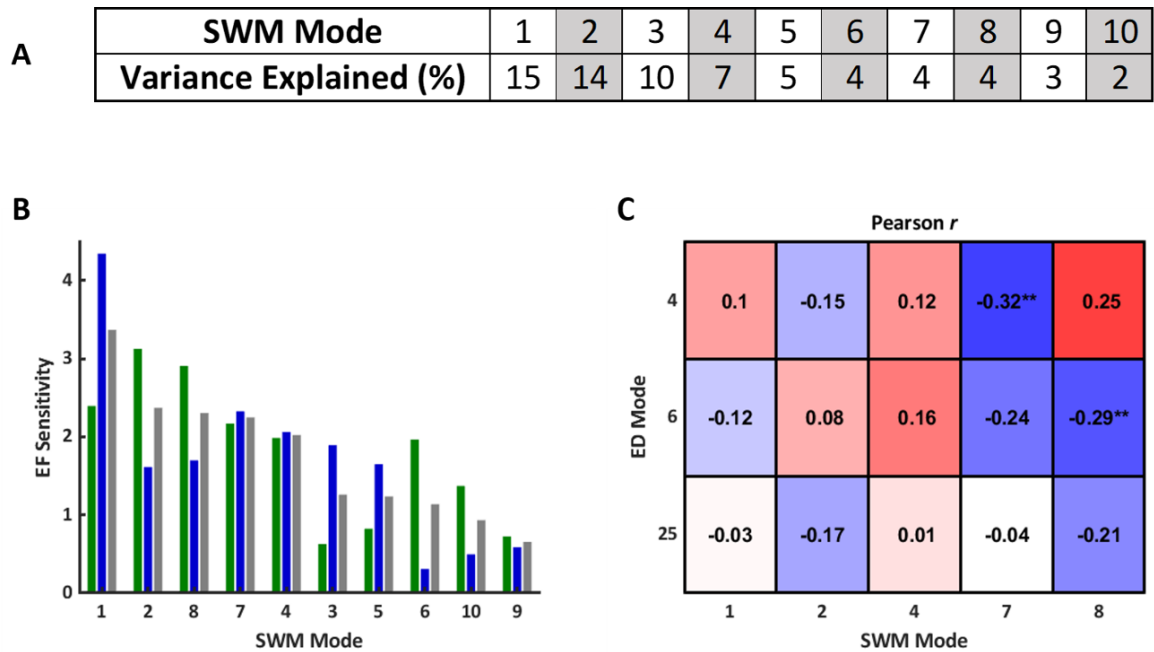
Figure 3.1. A) Variance explained (%) per SWM mode. **B)** Magnitude of the sensitivity of LV EF (green), RV EF (blue), and combined LV/RV EF (grey) to variations in SWM modes (pp/SD). SWM modes were ranked from greatest to least effect on combined LV/RV EF. **C)** Correlations between clinically significant ED shape modes and SWM modes that had the greatest effect on combined LV/RV EF. Symbols indicate statistical significance (**p<0.01). EF: ejection fraction; ED: end-diastolic; SWM: systolic wall motion.
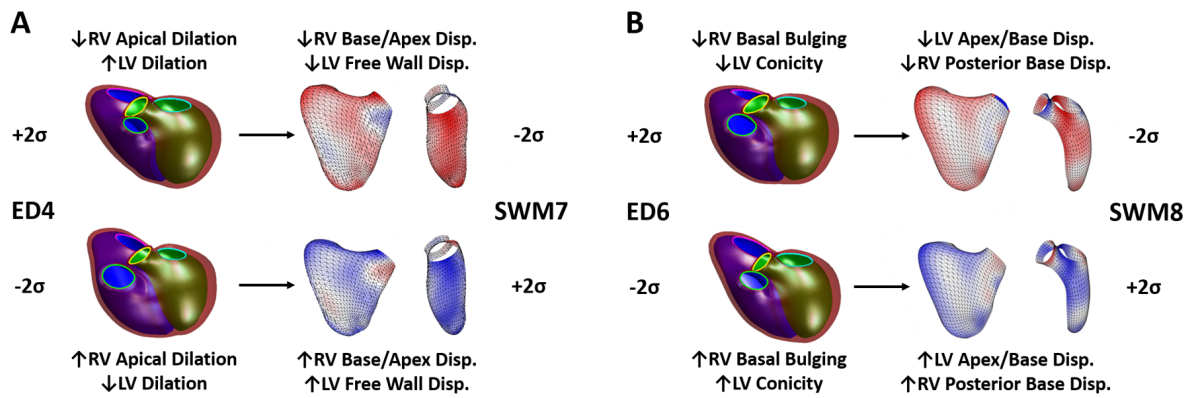
Figure 3.2. Summary morphological characteristics for associations between ED shape and SWM, **(A)** ED4 ∝ SWM7 and **(B)** ED6 ∝ SWM8. For ED shape modes, the LV endocardial surface, RV endocardial surface, and epicardial surface are shown in green, blue, and maroon, respectively, and the mitral, tricuspid, aortic, and pulmonary valves are shown in cyan, pink, yellow, and green, respectively. For SWM modes, the LV and RV free walls are shown and are colored based on the systolic displacement relative to the mean, inward (blue) and outward (red). ED: end-diastolic; LV: left ventricular; RV: right ventricular; SWM: systolic wall motion.
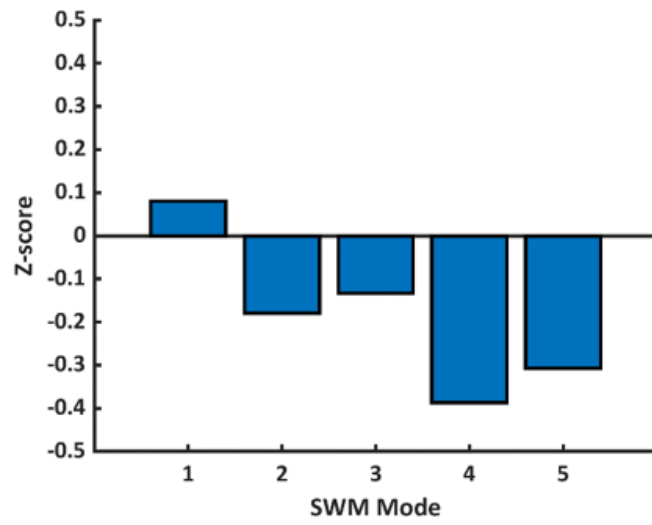
Figure 3.3. Difference between mean FE-computed model (blue bar) and atlas model (black line) SWM Z-scores. SWM: systolic wall motion.

ED4

ED · ES

ED6

ED · ES

+2σ

LV EF = 45.6% RV EF = 40.8%

+2σ

LV EF = 49.6% RV EF = 43.0%

-2σ

LV EF = 50.9% RV EF = 41.0%

-2σ

LV EF = 46.4% RV EF = 39.9%
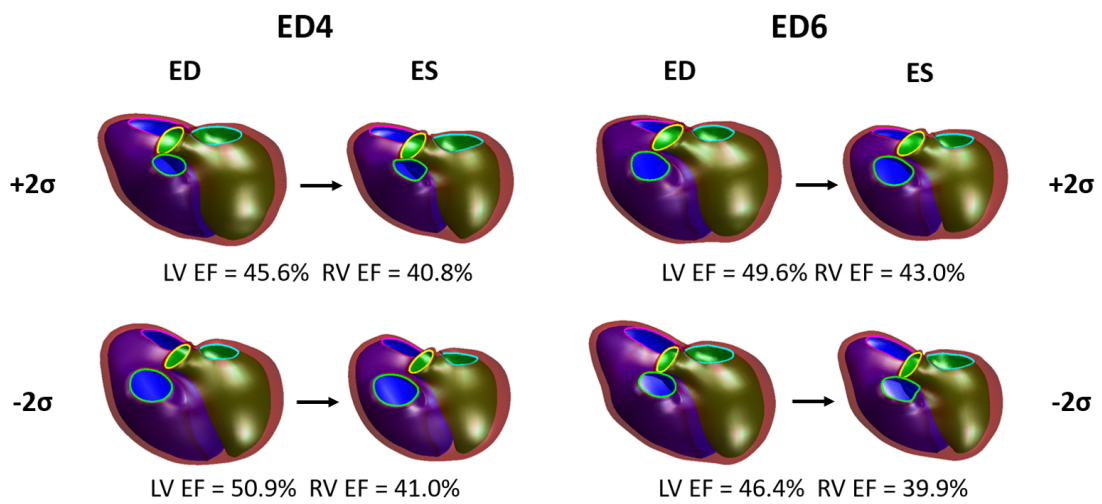
Figure 3.4. FE-computed ED shape perturbations with corresponding deformed ES shapes. Computed LV and RV EFs for each shape perturbation are also shown. For all models, the LV endocardial surface, RV endocardial surface, and epicardial surface are shown in green, blue, and maroon, respectively, and the mitral, tricuspid, aortic, and pulmonary valves are shown in cyan, pink, yellow, and green, respectively. EF: ejection fraction; ED: end-diastolic; ES: end-systolic; LV: left ventricular; RV: right ventricular.
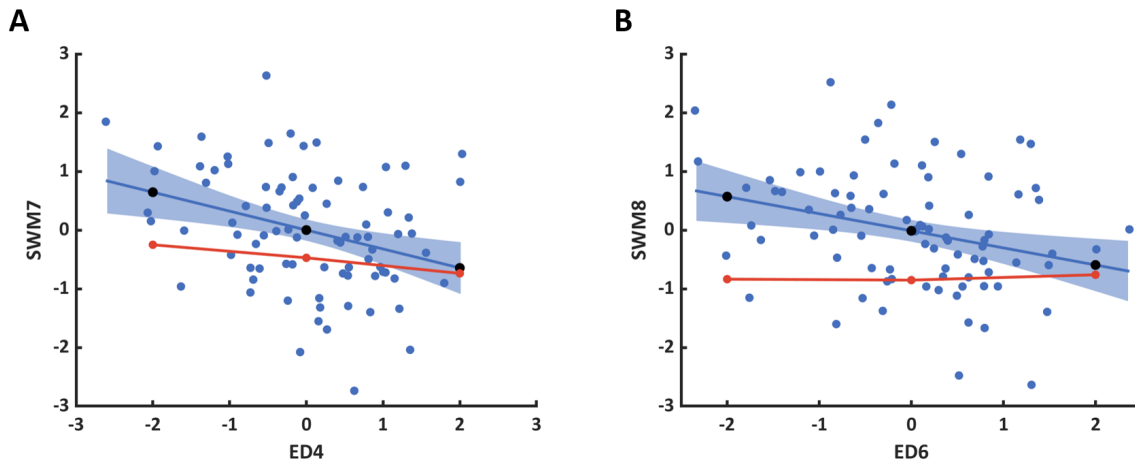
Figure 3.5. Comparison of predicted (black circles) and FE-computed (red line and circles) SWM Z-scores for shape perturbations along **(A)** ED4 ∝ SWM7 and **(B)** ED6 ∝ SWM8 using mean material properties. Significant ED shape mode and SWM mode correlations from patient data (blue circles) are represented as linear regression models with the fit (blue line) and 95% confidence intervals (blue shaded area). ED: end-diastolic; SWM: systolic wall motion.
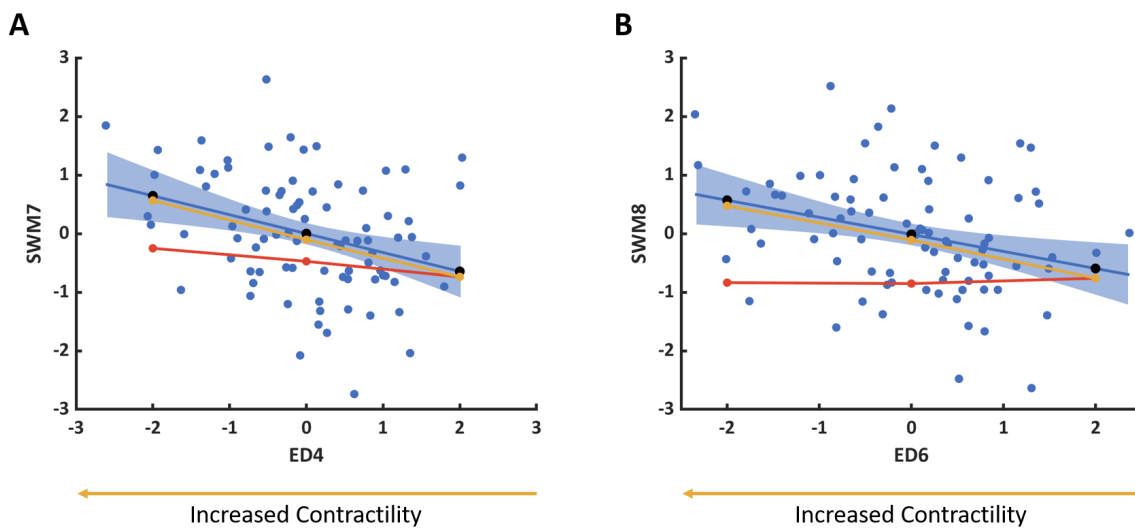
Figure 3.6. FE-computed changes in SWM Z-scores for shape perturbations along **(A)** ED4 ∝ SWM7 and **(B)** ED6 ∝ SWM8 with altered contractility (yellow line and circles) overlaid on Figure 3.5. The direction of ED shape variation associated with increased contractility is also shown. ED: end-diastolic; SWM: systolic wall motion.

Chapter 4

Conclusion

4.1　Summary

In this dissertation, we employed machine learning to enhance the throughput of cardiac shape modeling and demonstrated its use for the computational analysis of biventricular shape and mechanics in tetralogy of Fallot (TOF) to discover atlas-based biomarkers that can aid clinical prognosis and provide insight into the mechanisms of adverse ventricular remodeling and corresponding ventricular dysfunction.

In Chapter 1, we used deep learning to automate all of the major steps involved in constructing, three-dimensional biventricular shape models from raw cardiovascular magnetic resonance (CMR) image datasets. We developed the automated cardiac shape modeling pipeline as a series of five steps for view classification, slice selection, phase selection, anatomical landmark localization, and myocardial image segmentation to (1) allow the user to understand the purpose of each step rather than the pipeline appearing as a black box and (2) give the user the ability to make manual corrections at each step if necessary. We demonstrated this fully automated approach in a multi-institutional, international cohort of patients with repaired tetralogy of Fallot (rTOF, n=123), a patient population with particularly challenging anatomy. Overall, the automated pipeline performed well on an independent, multi-institutional test set that included a variety of CMR scanners, including several models that were not included in the training data. With this new automated pipeline, a single cardiac shape model can be made

in approximately 5 minutes, compared to the 60-90 minutes it would take an expert analyst to do so manually. To our knowledge, this is the first fully automated, end-to-end pipeline that can robustly create shape models for the challenging anatomies present in rTOF. With this approach, we can greatly reduce the manual input required to create shape models enabling the rapid analysis of largescale datasets and the potential to deploy statistical atlas-based analyses in point-of-care clinical settings.

In Chapter 2, we used statistical shape modeling to condense the wealth of morphological data from CMR imaging into quantitative, interpretable markers of regional biventricular shape in a rTOF patient cohort (n=84). Our aim was to discover atlas-based biomarkers that could characterize salient differences in adverse ventricular remodeling and aid clinical prognosis. Specifically, we tested the hypothesis that distinct markers of biventricular shape may discriminate differences between rTOF patients who did and did not require subsequent pulmonary valve replacement (PVR) better than standard imaging indices. We found three shape modes that were significantly associated with PVR status that were specific markers of opposing right ventricular (RV) apical dilation and left ventricular (LV) dilation, RV basal bulging and LV conicity, and pulmonary valve dilation. Patients in the PVR cohort demonstrated increased RV basal bulging and pulmonary valve dilation, which was associated with reduced RV and LV radial strain, while patients in the No-PVR cohort demonstrated increased RV apical dilation, which was associated with increased RV radial strain. We also found that these biventricular shape modes discriminated PVR status better than standard imaging indices, despite the fact that these indices are currently the cornerstone of clinical evaluation for PVR. Overall, these regional features of cardiac morphology may provide insight into adaptive vs. maladaptive types of structural remodeling and point toward an improved quantitative, patient-specific assessment tool for clinical use.

In Chapter 3, we used finite element models of biventricular biomechanics to investigate the extent to which clinically significant variations in ventricular shape discovered in Chapter 2, explain corresponding differences in ventricular function. Specifically, we tested the hypothesis

that shape variations can be direct determinants of variations in systolic function, but may also be indirect markers of altered myocardial mechanical properties that could help stratify clinical outcomes in rTOF. Prior to testing mechanistic relationships between features of cardiac shape, function, and intrinsic myocardial mechanical properties, we identified significant correlations between biventricular shape modes discovered in Chapter 2 and components of systolic wall motion that contributed most to differences in LV and RV ejection fraction. Upon examining these relationships in a finite element mechanics framework, we found that variations in shape explained differences in systolic function to varying degrees. In the case of RV apical dilation and LV dilation, we found that differences in the shape alone partially explained observed differences in systolic function, and after altering myocardial material properties, we found that greater RV apical dilation and less LV dilation were associated with increased RV basal and apical contractility. Given these results, we hypothesize that greater RV apical dilation may be a surrogate for increased RV basal and apical contractility that may serve as a compensatory mechanism to prevent LV dilation and preserve LV function; this mechanism may explain why patients with rTOF that had greater RV apical dilation and less LV dilation tended to have better prognoses. Overall, patients with rTOF may benefit from an atlas-based analysis of biventricular mechanics that can provide mechanistic insight into underlying myocardial pathophysiology and aid long-term clinical management.

4.2 Future Work

While this dissertation has made several advancements regarding the computational analysis of biventricular shape and mechanics for the discovery of clinically significant atlas-based biomarkers in rTOF, future work is imperative for the successful implementation of atlas-based analyses in the clinic to have real impact on patient management and outcomes. In the clinical translational process, there are typically two types of studies that are performed to validate new technologies and discoveries, retrospective and prospective, that can be performed either

cross-sectionally or longitudinally. The studies presented in this dissertation were retrospective in nature and, as a consequence, the clinical data available were heterogeneous and limited in clinical indicators such as exercise capacity, rhythm disturbances, and functional scores. In the future, prospective studies should be conducted that standardize the acquisition of these indicators before and after PVR with routine intervals of follow-up. This would be particularly useful for quantifying atlas-based biomarker relationships with differences in objective measures of outcome before and after PVR, rather than the decision to perform PVR itself. Additionally, the studies presented in this dissertation were cross-sectional in nature. In the future, longitudinal studies should be conducted to evaluate the temporal evolution of atlas-based biomarkers to get a better understanding of the time history of ventricular remodeling and how this relates to the optimal timing of PVR. By performing prospective and longitudinal studies, the atlas-based biomarkers discovered in this dissertation can be further evaluated regarding their sensitivity as indicators for the decision and timing of PVR and to assess long-term outcome. Only after assessing the effectiveness of atlas-based biomarkers for risk stratification in these additional studies can atlas-based analyses and their discoveries be subject to FDA approval and integrated with the clinical gold standard of care.

Additionally, the work presented in this dissertation primarily focused on developing a framework for the computational analysis of shape-function relationships in rTOF, but there are several other factors that are important to consider in order to get a comprehensive understanding of disease pathophysiology. One set of these factors include patient factors such as genetic markers, sex, and surgical history. Future work can explore atlas-based biomarker relationships with these patient factors to gain insight into whether a given individual may have a predisposition for a certain disease phenotype. This can in turn be used to guide early clinical management from the time of birth to surgical repair and establish an appropriate frequency for follow-up visits thereafter. In addition to patient factors, there are other physiological phenomenon that are pertinent in rTOF that the work presented in this dissertation did not examine including the contribution of variations in electrophysiology, scarring, and hemodynamics. Future work can

extend the computational modeling efforts outlined in this dissertation to include electromechanical coupling and a coupled hemodynamic model in the finite element analysis framework to get a better understanding of how differences in activation patterns or RV pressures might affect LV/RV ventricular interactions and function.

Finally, continual effort should be made to aggregate additional imaging and clinical datasets to increase the statistical power of atlas-based analyses and better represent variation in the rTOF population. Future studies should employ the automated cardiac shape modeling pipeline presented in this dissertation to analyze large patient cohorts from burgeoning collaborations with the SCMR registry, UK Biobank, INDICATOR study, etc. that have on the order of 500-1,000 patient datasets each. With this transition towards big-data population studies, future efforts should also be made to scale data storage and analysis techniques accordingly. This includes continual development of the Cardiac Atlas Project (CAP) database (https://capchd.ucsd.edu) and eventual hosting on the American Heart Association Precision Medicine Platform (https://precision.heart.org). Future development should ensure that the database is easy to credential and access and dynamic to allow for new clinical data types to be stored as they are acquired. When fully developed, the CAP database will facilitate collaborative atlas-based analyses of cardiac shape and mechanics among normal and pathological patient populations in addition to TOF and other congenital heart diseases, between clinicians and researchers. Along with infrastructure developments, future efforts should also focus on parallelizing solvers used for finite element analysis and machine learning techniques to allow them to be deployed on cloud-based computing platforms for optimal big data analysis.

4.3   Final Remarks

Altogether the work presented in this dissertation lays the groundwork for the computational analysis of biventricular shape and mechanics in rTOF and demonstrates the utility of atlas-based analyses in identifying more specific markers of adverse ventricular remodeling

that can supplement clinical decision making and provide insight into mechanisms underlying myocardial pathophysiology. In addition, this dissertation presents a fully automated, end-to-end pipeline for cardiac shape modeling that can be used to extend the atlas-based analyses presented herein to larger patient cohorts in order to further test and validate the atlas-based biomarkers discovered in this work. Ultimately, this precision medicine-based approach has great potential to serve as a valuable clinical tool that can improve diagnosis, prognosis, and treatment of individuals with TOF and other cardiac diseases.

Bibliography

[1] F. Bailliard, R. H. Anderson, Tetralogy of fallot, Orphanet J Rare Dis 4 (2009) 2. `doi: 10.1186/1750-1172-4-2`.

[2] D. van der Linde, E. E. Konings, M. A. Slager, M. Witsenburg, W. A. Helbing, J. J. Takkenberg, J. W. Roos-Hesselink, Birth prevalence of congenital heart disease worldwide: a systematic review and meta-analysis, J Am Coll Cardiol 58 (21) (2011) 2241–7. `doi: 10.1016/j.jacc.2011.08.025`.

[3] E. Fallot, Contribution a lanatomie pathologique de la maladie bleue (cyanotic cardiaque), Marseille méd 25 (1888) 77–138.

[4] C. W. Lillehei, M. Cohen, H. E. Warden, R. C. Read, J. B. Aust, R. A. Dewall, R. L. Varco, Direct vision intracardiac surgical correction of the tetralogy of fallot, pentalogy of fallot, and pulmonary atresia defects; report of first ten cases, Ann Surg 142 (3) (1955) 418–42. `doi:10.1097/00000658-195509000-00010`.

[5] M. D. Wolf, B. Landtman, C. A. Neill, H. B. Taussig, Total correction of tetralogy of fallot. i. follow-up study of 104 cases, Circulation 31 (1965) 385–93. `doi:10.1161/01.cir.31.3.385`.

[6] J. W. Kirklin, R. B. Wallace, D. C. McGoon, J. W. DuShane, Early and late results after intracardiac repair of tetralogy of fallot. 5-year review of 337 patients, Ann Surg 162 (4) (1965) 578–89. `doi:10.1097/00000658-196510000-00004`.

[7] B. S. Goldman, W. T. Mustard, G. S. Trusler, Total correction of tetralogy of fallot. review of ten years' experience, Br Heart J 30 (4) (1968) 563–8. `doi:10.1136/hrt.30.4.563`.

[8] H. Azar, R. L. Hardesty, R. G. Pontius, J. R. Zuberbuhler, H. T. Bahnson, A review of total correction in 200 cases of tetralogy of fallot, Arch Surg 99 (2) (1969) 281–5. `doi:10.1001/archsurg.1969.01340140153023`.

[9] T. R. Karl, S. Sano, S. Pornviliwan, R. B. Mee, Tetralogy of fallot: favorable outcome of nonneonatal transatrial, transpulmonary repair, Ann Thorac Surg 54 (5) (1992) 903–7. `doi:10.1016/0003-4975(92)90646-l`.

[10] J. Fraser, C. D., E. D. McKenzie, D. A. Cooley, Tetralogy of fallot: surgical management individualized to the patient, Ann Thorac Surg 71 (5) (2001) 1556–61; discussion 1561–3. `doi:10.1016/s0003-4975(01)02475-4`.

[11] S. E. Luijnenburg, W. A. Helbing, A. Moelker, L. J. Kroft, M. Groenink, J. W. Roos-Hesselink, Y. B. de Rijke, M. G. Hazekamp, A. J. Bogers, H. W. Vliegen, B. J. Mulder, 5-year serial follow-up of clinical condition and ventricular function in patients after repair of tetralogy of fallot, Int J Cardiol 169 (6) (2013) 439–44. `doi:10.1016/j.ijcard.2013.10.013`.

[12] C. D. Mavroudis, J. Frost, C. Mavroudis, Pulmonary valve preservation and restoration strategies for repair of tetralogy of fallot, Cardiol Young 24 (6) (2014) 1088–94. `doi:10.1017/s1047951114001991`.

[13] V. L. Vida, A. Guariento, F. Zucchetta, M. Padalino, B. Castaldi, O. Milanesi, G. Stellin, Preservation of the pulmonary valve during early repair of tetralogy of fallot: Surgical techniques, Semin Thorac Cardiovasc Surg Pediatr Card Surg Annu 19 (1) (2016) 75–81. `doi:10.1053/j.pcsu.2015.12.008`.

[14] L. Sasson, S. Houri, A. Raucher Sternfeld, I. Cohen, O. Lenczner, E. L. Bove, L. Kapusta, A. Tamir, Right ventricular outflow tract strategies for repair of tetralogy of fallot: effect of monocusp valve reconstruction, Eur J Cardiothorac Surg 43 (4) (2013) 743–51. `doi:10.1093/ejcts/ezs479`.

[15] K. H. Choi, S. C. Sung, H. Kim, H. D. Lee, G. Kim, H. Ko, Late results of right ventricular outflow tract reconstruction with a bicuspid expanded polytetrafluoroethylene valved conduit, J Card Surg 33 (1) (2018) 36–40. `doi:10.1111/jocs.13507`.

[16] C. W. Mercer, S. C. West, M. S. Sharma, M. Yoshida, V. O. Morell, Polytetrafluoroethylene conduits versus homografts for right ventricular outflow tract reconstruction in infants and young children: An institutional experience, J Thorac Cardiovasc Surg 155 (5) (2018) 2082–2091.e1. `doi:10.1016/j.jtcvs.2017.11.107`.

[17] S. M. Yuan, A. Shinfeld, E. Raanani, The blalock-taussig shunt, J Card Surg 24 (2) (2009) 101–8. `doi:10.1111/j.1540-8191.2008.00758.x`.

[18] C. A. Smith, C. McCracken, A. S. Thomas, L. G. Spector, J. D. St Louis, M. E. Oster, J. H. Moller, L. Kochilas, Long-term outcomes of tetralogy of fallot: A study from the pediatric cardiac care consortium, JAMA Cardiology 4 (1) (2019) 34–41. `doi:10.1001/jamacardio.2018.4255`.

[19] A. Cedars, L. Benjamin, R. Vyhmeister, K. Harris, E. A. Bradley, S. Wadia, A. J. Awad, E. Novak, Contemporary hospitalization rate among adults with complex congenital heart disease, World J Pediatr Congenit Heart Surg 7 (3) (2016) 334–43. `doi:10.1177/2150135116639541`.

[20] M. Gilboa Suzanne, J. Devine Owen, E. Kucik James, E. Oster Matthew, T. Riehle-Colarusso, N. Nembhard Wendy, P. Xu, A. Correa, K. Jenkins, J. Marelli Ariane, Congenital heart defects in the united states, Circulation 134 (2) (2016) 101–109. `doi:10.1161/CIRCULATIONAHA.115.019307`.

[21] H. Kim, S. C. Sung, S. H. Kim, Y. H. Chang, H. D. Lee, J. A. Park, Y. S. Lee, Early and late outcomes of total repair of tetralogy of fallot: risk factors for late right ventricular dilatation, Interact Cardiovasc Thorac Surg 17 (6) (2013) 956–62. `doi:10.1093/icvts/ivt361`.

[22] P. G. Sfyridis, G. V. Kirvassilis, J. K. Papagiannis, D. P. Avramidis, C. G. Ieromonachos, P. N. Zavaropoulos, G. E. Sarris, Preservation of right ventricular structure and function following transatrial-transpulmonary repair of tetralogy of fallot, Eur J Cardiothorac Surg 43 (2) (2013) 336–42. `doi:10.1093/ejcts/ezs221`.

[23] E. Mouws, N. M. S. de Groot, P. C. van de Woestijne, P. L. de Jong, W. A. Helbing, I. M. van Beynum, A. Bogers, Tetralogy of fallot in the current era, Semin Thorac Cardiovasc Surg 31 (3) (2019) 496–504. `doi:10.1053/j.semtcvs.2018.10.015`.

[24] B. Bouzas, P. J. Kilner, M. A. Gatzoulis, Pulmonary regurgitation: not a benign lesion, Eur Heart J 26 (5) (2005) 433–9. `doi:10.1093/eurheartj/ehi091`.

[25] A. N. Redington, Physiopathology of right ventricular failure, Semin Thorac Cardiovasc Surg Pediatr Card Surg Annu (2006) 3–10. `doi:10.1053/j.pcsu.2006.02.005`.

[26] A. S. Mueller, D. M. McDonald, H. S. Singh, J. N. Ginns, Heart failure in adult congenital heart disease: tetralogy of fallot, Heart Fail Rev 25 (4) (2020) 583–598. `doi:10.1007/s10741-019-09903-0`.

[27] V. Changela, C. John, S. Maheshwari, Unusual cardiac associations with tetralogy of fallot—a descriptive study, Pediatric Cardiology 31 (6) (2010) 785–791. `doi:10.1007/s00246-010-9701-1`.

[28] V. Sharma, E. R. Griffiths, A. W. Eckhauser, R. G. Gray, M. H. Martin, C. Zhang, A. P. Presson, P. T. Burch, Pulmonary valve replacement: A single-institution comparison of surgical and transcatheter valves, Ann Thorac Surg 106 (3) (2018) 807–813. `doi:10.1016/j.athoracsur.2018.04.002`.

[29] J. P. G. van der Ven, E. van den Bosch, A. J. C. C. Bogers, W. A. Helbing, Current outcomes and treatment of tetralogy of fallot, F1000Research 8 (2019) F1000 Faculty Rev–1530. `doi:10.12688/f1000research.17174.1`.

[30] H. Baumgartner, P. Bonhoeffer, N. M. De Groot, F. de Haan, J. E. Deanfield, N. Galie, M. A. Gatzoulis, C. Gohlke-Baerwolf, H. Kaemmerer, P. Kilner, F. Meijboom, B. J. Mulder, E. Oechslin, J. M. Oliver, A. Serraf, A. Szatmari, E. Thaulow, P. R. Vouhe, E. Walma, Esc guidelines for the management of grown-up congenital heart disease, Eur Heart J 31 (23) (2010) 2915–57. `doi:10.1093/eurheartj/ehq249`.

[31] C. K. Silversides, M. Kiess, L. Beauchesne, T. Bradley, M. Connelly, K. Niwa, B. Mulder, G. Webb, J. Colman, J. Therrien, Canadian cardiovascular society 2009 consensus conference on the management of adults with congenital heart disease: outflow tract obstruction, coarctation of the aorta, tetralogy of fallot, ebstein anomaly and marfan's syndrome, Can J Cardiol 26 (3) (2010) e80–97. `doi:10.1016/s0828-282x(10)70355-x`.

[32] C. A. Warnes, R. G. Williams, T. M. Bashore, J. S. Child, H. M. Connolly, J. A. Dearani, P. Del Nido, J. W. Fasules, J. Graham, T. P., Z. M. Hijazi, S. A. Hunt, M. E. King, M. J. Landzberg, P. D. Miner, M. J. Radford, E. P. Walsh, G. D. Webb, Acc/aha 2008 guidelines for the management of adults with congenital heart disease, J Am Coll Cardiol 52 (23) (2008) e143–e263. `doi:10.1016/j.jacc.2008.10.001`.

[33] A. M. Valente, K. Gauvreau, G. E. Assenza, S. V. Babu-Narayan, J. Schreier, M. A. Gatzoulis, M. Groenink, R. Inuzuka, P. J. Kilner, Z. Koyak, M. J. Landzberg, B. Mulder, A. J. Powell, R. Wald, T. Geva, Contemporary predictors of death and sustained ventricular tachycardia in patients with repaired tetralogy of fallot enrolled in the indicator cohort, Heart 100 (3) (2014) 247–53. `doi:10.1136/heartjnl-2013-304958`.

[34] S. Sarikouch, D. Boethig, P. Beerbaum, Gender-specific algorithms recommended for patients with congenital heart defects: review of the literature, Thorac Cardiovasc Surg 61 (1) (2013) 79–84. `doi:10.1055/s-0032-1326774`.

[35] K. Zervan, C. Male, T. Benesch, U. Salzer-Muhar, Ventricular interaction in children after repair of tetralogy of fallot: a longitudinal echocardiographic study, Eur J Echocardiogr 10 (5) (2009) 641–6. `doi:10.1093/ejechocard/jep025`.

[36] J. T. Tretter, A. N. Redington, The forgotten ventricle? the left ventricle in right-sided congenital heart disease, Circ Cardiovasc Imaging 11 (3) (2018) e007410. `doi:10.1161/circimaging.117.007410`.

[37] T. Geva, Repaired tetralogy of fallot: the roles of cardiovascular magnetic resonance in evaluating pathophysiology and for pulmonary valve replacement decision support, J Cardiovasc Magn Reson 13 (2011) 9. `doi:10.1186/1532-429x-13-9`.

[38] H. N. Ntsinjana, M. L. Hughes, A. M. Taylor, The role of cardiovascular magnetic resonance in pediatric congenital heart disease, J Cardiovasc Magn Reson 13 (2011) 51. `doi:10.1186/1532-429x-13-51`.

[39] P. Medrano-Gracia, B. R. Cowan, B. Ambale-Venkatesh, D. A. Bluemke, J. Eng, J. P. Finn, C. G. Fonseca, J. A. Lima, A. Suinesiaputra, A. A. Young, Left ventricular shape variation in asymptomatic populations: the multi-ethnic study of atherosclerosis, J Cardiovasc Magn Reson 16 (2014) 56. `doi:10.1186/s12968-014-0056-2`.

[40] W. Bai, W. Shi, A. de Marvao, T. J. Dawes, D. P. O'Regan, S. A. Cook, D. Rueckert, A bi-ventricular cardiac atlas built from 1000+ high resolution mr images of healthy subjects and an analysis of shape and motion, Med Image Anal 26 (1) (2015) 133–45. `doi:10.1016/j.media.2015.08.009`.

[41] G. Farrar, A. Suinesiaputra, K. Gilbert, J. C. Perry, S. Hegde, A. Marsden, A. A. Young, J. H. Omens, A. D. McCulloch, Atlas-based ventricular shape analysis for understanding congenital heart disease, Prog Pediatr Cardiol 43 (2016) 61–69. `doi:10.1016/j.ppedcard.2016.07.010`.

[42] K. Gilbert, N. Forsch, S. Hegde, C. Mauger, J. H. Omens, J. C. Perry, B. Pontre, A. Suine-siaputra, A. A. Young, A. D. McCulloch, Atlas-based computational analysis of heart shape and function in congenital heart disease, J Cardiovasc Transl Res 11 (2) (2018) 123–132. `doi:10.1007/s12265-017-9778-5.`

[43] A. Suinesiaputra, P. Ablin, X. Alba, M. Alessandrini, J. Allen, W. Bai, S. Cimen, P. Claes, B. R. Cowan, J. D'Hooge, N. Duchateau, J. Ehrhardt, A. F. Frangi, A. Gooya, V. Grau, K. Lekadir, A. Lu, A. Mukhopadhyay, I. Oksuz, N. Parajali, X. Pennec, M. Pereanez, C. Pinto, P. Piras, M. M. Rohe, D. Rueckert, D. Saring, M. Sermesant, K. Siddiqi, M. Tabassian, L. Teresi, S. A. Tsaftaris, M. Wilms, A. A. Young, X. Zhang, P. Medrano-Gracia, Statistical shape modeling of the left ventricle: myocardial infarct classification challenge, IEEE J Biomed Health Inform 22 (2) (2018) 503–515. `doi:10.1109/jbhi.2017.2652449.`

[44] K. Gilbert, W. Bai, C. Mauger, P. Medrano-Gracia, A. Suinesiaputra, A. M. Lee, M. M. Sanghvi, N. Aung, S. K. Piechnik, S. Neubauer, S. E. Petersen, D. Rueckert, A. A. Young, Independent left ventricular morphometric atlases show consistent relationships with cardiovascular risk factors: A uk biobank study, Sci Rep 9 (1) (2019) 1130. `doi:10.1038/s41598-018-37916-6.`

[45] H. K. Narayan, R. Xu, N. Forsch, S. Govil, D. Iukuridze, L. Lindenfeld, E. Adler, S. Hegde, A. Tremoulet, B. Ky, S. Armenian, J. Omens, A. D. McCulloch, Atlas-based measures of left ventricular shape may improve characterization of adverse remodeling in anthracycline-exposed childhood cancer survivors: a cross-sectional imaging study, Cardiooncology 6 (2020) 13. `doi:10.1186/s40959-020-00069-5.`

[46] K. P. Vincent, N. Forsch, S. Govil, J. M. Joblon, J. H. Omens, J. C. Perry, A. D. McCulloch, Atlas-based methods for efficient characterization of patient-specific ventricular activation patterns, EP Europace 23 (Supplement1) (2021) i88–i95. `doi:10.1093/europace/euaa397.`

[47] C. A. Mauger, S. Govil, R. Chabiniok, K. Gilbert, S. Hegde, T. Hussain, A. D. McCulloch, C. J. Occleshaw, J. Omens, J. C. Perry, K. Pushparajah, A. Suinesiaputra, L. Zhong, A. A. Young, Right-left ventricular shape variations in tetralogy of fallot: associations with pulmonary regurgitation, J Cardiovasc Magn Reson 23 (1) (2021) 105. `doi:10.1186/s12968-021-00780-x.`

[48] S. Govil, N. Forsch, S. Salehyar, K. Gilbert, A. Suinesiaputra, S. Hegde, J. C. Perry, A. A. Young, J. H. Omens, A. D. McCulloch, Morphological markers and determinants of left ventricular systolic dysfunction in repaired tetralogy of fallot, in: ASME 2021 International Mechanical Engineering Congress and Exposition, Vol. Volume 5: Biomedical and Biotechnology, 2021. `doi:10.1115/imece2021-70591.`

[49] A. Elsayed, C. A. Mauger, E. Ferdian, K. Gilbert, M. Scadeng, C. J. Occleshaw, B. S. Lowe, A. D. McCulloch, J. H. Omens, S. Govil, K. Pushparajah, A. A. Young, Right ventricular flow vorticity relationships with biventricular shape in adult tetralogy of fallot, Frontiers in Cardiovascular Medicine 8 (2022). `doi:10.3389/fcvm.2021.806107.`

[50] A. Mîra, P. Lamata, K. Pushparajah, G. Abraham, C. A. Mauger, A. D. McCulloch, J. H. Omens, M. M. Bissell, Z. Blair, T. Huffaker, A. Tandon, S. Engelhardt, S. Koehler, T. Pickardt, P. Beerbaum, S. Sarikouch, H. Latus, G. Greil, A. A. Young, T. Hussain, Le cœur en sabot: shape associations with adverse events in repaired tetralogy of fallot, J Cardiovasc Magn Reson 24 (1) (2022) 46. `doi:10.1186/s12968-022-00877-x`.

[51] S. Govil, S. Hegde, J. C. Perry, J. H. Omens, A. D. McCulloch, An atlas-based analysis of biventricular mechanics in tetralogy of fallot, in: O. Camara, E. Puyol-Antón, C. Qin, M. Sermesant, A. Suinesiaputra, S. Wang, A. Young (Eds.), Statistical Atlases and Computational Models of the Heart. Regular and CMRxMotion Challenge Papers, Springer Nature Switzerland, pp. 112–122. `doi:10.1007/978-3-031-23443-9_11`.

[52] S. Govil, C. Mauger, S. Hegde, C. J. Occleshaw, X. Yu, J. C. Perry, A. A. Young, J. H. Omens, A. D. McCulloch, Biventricular shape modes discriminate pulmonary valve replacement in tetralogy of fallot better than imaging indices, Sci Rep 13 (1) (2023) 2335. `doi:10.1038/s41598-023-28358-w`.

[53] A. A. Young, B. R. Cowan, S. F. Thrupp, W. J. Hedley, L. J. Dell'Italia, Left ventricular mass and volume: fast calculation with guide-point modeling on mr images, Radiology 216 (2) (2000) 597–602. `doi:10.1148/radiology.216.2.r00au14597`.

[54] B. Li, Y. Liu, C. J. Occleshaw, B. R. Cowan, A. A. Young, In-line automated tracking for ventricular function with magnetic resonance imaging, JACC Cardiovasc Imaging 3 (8) (2010) 860–6. `doi:10.1016/j.jcmg.2010.04.013`.

[55] K. Gilbert, H. I. Lam, B. Pontré, B. R. Cowan, C. J. Occleshaw, J. Y. Liu, A. A. Young, An interactive tool for rapid biventricular analysis of congenital heart disease, Clin Physiol Funct Imaging 37 (4) (2017) 413–420. `doi:10.1111/cpf.12319`.

[56] K. Gilbert, B. Pontre, C. J. Occleshaw, B. R. Cowan, A. Suinesiaputra, A. A. Young, 4d modelling for rapid assessment of biventricular function in congenital heart disease, Int J Cardiovasc Imaging 34 (3) (2018) 407–417. `doi:10.1007/s10554-017-1236-6`.

[57] G. Litjens, T. Kooi, B. E. Bejnordi, A. A. A. Setio, F. Ciompi, M. Ghafoorian, J. van der Laak, B. van Ginneken, C. I. Sánchez, A survey on deep learning in medical image analysis, Med Image Anal 42 (2017) 60–88. `doi:10.1016/j.media.2017.07.005`.

[58] C. Chen, C. Qin, H. Qiu, G. Tarroni, J. Duan, W. Bai, D. Rueckert, Deep learning for cardiac image segmentation: A review, Front Cardiovasc Med 7 (2020) 25. `doi:10.3389/fcvm.2020.00025`.

[59] C. G. Fonseca, M. Backhaus, D. A. Bluemke, R. D. Britten, J. D. Chung, B. R. Cowan, I. D. Dinov, J. P. Finn, P. J. Hunter, A. H. Kadish, D. C. Lee, J. A. C. Lima, P. Medrano-Gracia, K. Shivkumar, A. Suinesiaputra, W. Tao, A. A. Young, The cardiac atlas project - an imaging database for computational modeling and statistical atlases of the heart, Bioinformatics 27 (16) (2011) 2288–2295. `doi:10.1093/bioinformatics/btr360`.

[60] C. Mauger, K. Gilbert, A. Suinesiaputra, B. Pontre, J. Omens, A. McCulloch, A. Young, An iterative diffeomorphic algorithm for registration of subdivision surfaces: Application to congenital heart disease, Annu Int Conf IEEE Eng Med Biol Soc 2018 (2018) 596–599. `doi:10.1109/embc.2018.8512394`.

[61] C. Mauger, K. Gilbert, A. M. Lee, M. M. Sanghvi, N. Aung, K. Fung, V. Carapella, S. K. Piechnik, S. Neubauer, S. E. Petersen, A. Suinesiaputra, A. A. Young, Right ventricular shape and function: cardiovascular magnetic resonance reference morphology and biventricular risk factor morphometrics in uk biobank, J Cardiovasc Magn Reson 21 (1) (2019) 41. `doi:10.1186/s12968-019-0551-6`.

[62] E. S. Lane, N. Azarmehr, J. Jevsikov, J. P. Howard, M. J. Shun-shin, G. D. Cole, D. P. Francis, M. Zolgharni, Multibeat echocardiographic phase detection using deep neural networks, Computers in Biology and Medicine 133 (2021) 104373. `doi:10.1016/j.compbiomed.2021.104373`.

[63] N. Bahrami, T. Retson, K. Blansit, K. Wang, A. Hsiao, Automated selection of myocardial inversion time with a convolutional neural network: Spatial temporal ensemble myocardium inversion network (stemi-net), Magn Reson Med 81 (5) (2019) 3283–3291. `doi:10.1002/mrm.27680`.

[64] A. Suinesiaputra, A. D. McCulloch, M. P. Nash, B. Pontre, A. A. Young, Cardiac image modelling: Breadth and depth in heart disease, Med Image Anal 33 (2016) 38–43. `doi:10.1016/j.media.2016.06.027`.

[65] H. Xue, J. Artico, M. Fontana, J. C. Moon, R. H. Davies, P. Kellman, Landmark detection in cardiac mri by using a convolutional neural network, Radiol Artif Intell 3 (5) (2021) e200197. `doi:10.1148/ryai.2021200197`.

[66] O. Ronneberger, P. Fischer, T. Brox, U-net: Convolutional networks for biomedical image segmentation (2015). `doi:10.48550/ARXIV.1505.04597`.

[67] G. Klambauer, T. Unterthiner, A. Mayr, S. Hochreiter, Self-normalizing neural networks (2017). `doi:10.48550/ARXIV.1706.02515`.

[68] E. Heiberg, J. Sjögren, M. Ugander, M. Carlsson, H. Engblom, H. Arheden, Design and validation of segment - freely available software for cardiovascular image analysis, BMC Medical Imaging 10 (1) (2010) 1. `doi:10.1186/1471-2342-10-1`.

[69] F. Isensee, P. F. Jaeger, S. A. A. Kohl, J. Petersen, K. H. Maier-Hein, nnu-net: a self-configuring method for deep learning-based biomedical image segmentation, Nature Methods 18 (2) (2021) 203–211. `doi:10.1038/s41592-020-01008-z`.

[70] V. M. Campello, P. Gkontra, C. Izquierdo, C. Martín-Isla, A. Sojoudi, P. M. Full, K. Maier-Hein, Y. Zhang, Z. He, J. Ma, M. Parreño, A. Albiol, F. Kong, S. C. Shadden, J. C. Acero, V. Sundaresan, M. Saber, M. Elattar, H. Li, B. Menze, F. Khader, C. Haarburger, C. M. Scannell, M. Veta, A. Carscadden, K. Punithakumar, X. Liu, S. A. Tsaftaris,

X. Huang, X. Yang, L. Li, X. Zhuang, D. Viladés, M. L. Descalzo, A. Guala, L. L. Mura, M. G. Friedrich, R. Garg, J. Lebel, F. Henriques, M. Karakas, E. Çavuş, S. E. Petersen, S. Escalera, S. Seguí, J. F. Rodríguez-Palomares, K. Lekadir, Multi-centre, multi-vendor and multi-disease cardiac segmentation: The m&ms challenge, IEEE Transactions on Medical Imaging 40 (12) (2021) 3543–3554. `doi:10.1109/TMI.2021.3090082`.

[71] A. L. Maas, A. Y. Hannun, A. Y. Ng, Rectifier nonlinearities improve neural network acoustic models, in: Proc. icml, Vol. 30, 2013, p. 3.

[72] D. Ulyanov, A. Vedaldi, V. S. Lempitsky, Instance normalization: The missing ingredient for fast stylization (2016). `doi:10.48550/ARXIV.1607.08022`.

[73] M. Drozdzal, E. Vorontsov, G. Chartrand, S. Kadoury, C. Pal, The importance of skip connections in biomedical image segmentation, in: G. Carneiro, D. Mateus, L. Peter, A. Bradley, J. M. R. S. Tavares, V. Belagiannis, J. P. Papa, J. C. Nascimento, M. Loog, Z. Lu, J. S. Cardoso, J. Cornebise (Eds.), Deep Learning and Data Labeling for Medical Applications, Vol. 10008, 2016, pp. 179–187. `doi:10.1007/978-3-319-46976-8_19`.

[74] L.-C. Chen, G. Papandreou, I. Kokkinos, K. Murphy, A. L. Yuille, Deeplab: Semantic image segmentation with deep convolutional nets, atrous convolution, and fully connected crfs (2016). `doi:10.48550/ARXIV.1606.00915`.

[75] F. Milletari, N. Navab, S.-A. Ahmadi, V-net: Fully convolutional neural networks for volumetric medical image segmentation (2016). `doi:10.48550/ARXIV.1606.04797`.

[76] G. Rote, Computing the minimum hausdorff distance between two point sets on a line under translation, Information Processing Letters 38 (3) (1991) 123–127. `doi:10.1016/0020-0190(91)90233-8`.

[77] J. Duan, G. Bello, J. Schlemper, W. Bai, T. J. W. Dawes, C. Biffi, A. de Marvao, G. Doumoud, D. P. O'Regan, D. Rueckert, Automatic 3d bi-ventricular segmentation of cardiac images by a shape-refined multi- task deep learning approach, IEEE Trans Med Imaging 38 (9) (2019) 2151–2164. `doi:10.1109/tmi.2019.2894322`.

[78] A. Banerjee, J. Camps, E. Zacur, C. M. Andrews, Y. Rudy, R. P. Choudhury, B. Rodriguez, V. Grau, A completely automated pipeline for 3d reconstruction of human heart from 2d cine magnetic resonance slices, Philos Trans A Math Phys Eng Sci 379 (2212) (2021) 20200257. `doi:10.1098/rsta.2020.0257`.

[79] A. Suinesiaputra, C. A. Mauger, B. Ambale-Venkatesh, D. A. Bluemke, J. Dam Gade, K. Gilbert, M. H. A. Janse, L. S. Hald, C. Werkhoven, C. O. Wu, J. A. C. Lima, A. A. Young, Deep learning analysis of cardiac mri in legacy datasets: Multi-ethnic study of atherosclerosis, Front Cardiovasc Med 8 (2021) 807728. `doi:10.3389/fcvm.2021.807728`.

[80] J. Corral Acero, A. Schuster, E. Zacur, T. Lange, T. Stiermaier, S. J. Backhaus, H. Thiele, A. Bueno-Orovio, P. Lamata, I. Eitel, V. Grau, Understanding and improving risk assessment after myocardial infarction using automated left ventricular shape analysis, JACC Cardiovasc Imaging 15 (9) (2022) 1563–1574. `doi:10.1016/j.jcmg.2021.11.027`.

[81] S. E. Petersen, N. Aung, M. M. Sanghvi, F. Zemrak, K. Fung, J. M. Paiva, J. M. Francis, M. Y. Khanji, E. Lukaschuk, A. M. Lee, V. Carapella, Y. J. Kim, P. Leeson, S. K. Piechnik, S. Neubauer, Reference ranges for cardiac structure and function using cardiovascular magnetic resonance (cmr) in caucasians from the uk biobank population cohort, Journal of Cardiovascular Magnetic Resonance 19 (1) (2017) 18. `doi:10.1186/s12968-017-0327-9`.

[82] A. Dragulescu, L. Grosse-Wortmann, C. Fackoury, L. Mertens, Echocardiographic assessment of right ventricular volumes: a comparison of different techniques in children after surgical repair of tetralogy of fallot, Eur Heart J Cardiovasc Imaging 13 (7) (2012) 596–604. `doi:10.1093/ejechocard/jer278`.

[83] A. M. Valente, K. Gauvreau, G. E. Assenza, S. V. Babu-Narayan, S. P. Evans, M. Gatzoulis, M. Groenink, R. Inuzuka, P. J. Kilner, Z. Koyak, M. J. Landzberg, B. Mulder, A. J. Powell, R. Wald, T. Geva, Rationale and design of an international multicenter registry of patients with repaired tetralogy of fallot to define risk factors for late adverse outcomes: the indicator cohort, Pediatr Cardiol 34 (1) (2013) 95–104. `doi:10.1007/s00246-012-0394-5`.

[84] T. E. Downing, Y. Y. Kim, Tetralogy of fallot: General principles of management, Cardiology Clinics 33 (4) (2015) 531–541. `doi:10.1016/j.ccl.2015.07.002`.

[85] N. Dłużniewska, P. Podolec, M. Skubera, M. Smaś-Suska, J. Pająk, M. Urbańczyk-Zawadzka, W. Płazak, M. Olszowska, L. Tomkiewicz-Pająk, Long-term follow-up in adults after tetralogy of fallot repair, Cardiovascular Ultrasound 16 (1) (2018) 28–28. `doi:10.1186/s12947-018-0146-7`.

[86] E. L. Heng, M. A. Gatzoulis, A. Uebing, B. Sethia, H. Uemura, G. C. Smith, G. P. Diller, K. P. McCarthy, S. Y. Ho, W. Li, P. Wright, V. Spadotto, P. J. Kilner, P. Oldershaw, D. J. Pennell, D. F. Shore, S. V. Babu-Narayan, Immediate and midterm cardiac remodeling after surgical pulmonary valve replacement in adults with repaired tetralogy of fallot: A prospective cardiovascular magnetic resonance and clinical study, Circulation 136 (18) (2017) 1703–1713. `doi:10.1161/circulationaha.117.027402`.

[87] F. He, Z. Feng, Q. Chen, Y. Jiao, Z. Hua, H. Zhang, K. Yang, K. Pang, M. Lu, K. Ma, S. Zhang, L. Qi, G. Wang, S. Li, Whether pulmonary valve replacement in asymptomatic patients with moderate or severe regurgitation after tetralogy of fallot repair is appropriate: A case-control study, Journal of the American Heart Association 8 (1) (2019) e010689–e010689. `doi:10.1161/JAHA.118.010689`.

[88] W. Alkashkari, A. Alsubei, Z. M. Hijazi, Transcatheter pulmonary valve replacement: Current state of art, Current Cardiology Reports 20 (4) (2018) 27. `doi:10.1007/s11886-018-0966-y`.

[89] H. Tatewaki, A. Shiose, Pulmonary valve replacement after repaired tetralogy of fallot, General Thoracic and Cardiovascular Surgery 66 (9) (2018) 509–515. `doi:10.1007/s11748-018-0931-0`.

[90] D. Balzer, Pulmonary valve replacement for tetralogy of fallot, Methodist DeBakey cardiovascular journal 15 (2) (2019) 122–132. `doi:10.14797/mdcj-15-2-122`.

[91] C. Lee, Y. M. Kim, C.-H. Lee, J. G. Kwak, C. S. Park, J. Y. Song, W.-S. Shim, E. Y. Choi, S. Y. Lee, J. S. Baek, Outcomes of pulmonary valve replacement in 170 patients with chronic pulmonary regurgitation after relief of right ventricular outflow tract obstruction: Implications for optimal timing of pulmonary valve replacement, Journal of the American College of Cardiology 60 (11) (2012) 1005–1014. `doi:10.1016/j.jacc.2012.03.077`.

[92] J. P. Bokma, M. M. Winter, T. Oosterhof, H. W. Vliegen, A. P. van Dijk, M. G. Hazekamp, D. R. Koolbergen, M. Groenink, B. J. Mulder, B. J. Bouma, Preoperative thresholds for mid-to-late haemodynamic and clinical outcomes after pulmonary valve replacement in tetralogy of fallot, Eur Heart J 37 (10) (2016) 829–35. `doi:10.1093/eurheartj/ehv550`.

[93] T. Geva, Indications for pulmonary valve replacement in repaired tetralogy of fallot: the quest continues, Circulation 128 (17) (2013) 1855–1857. `doi:10.1161/CIRCULATIONAHA.113.005878`.

[94] F. H. Sheehan, S. Ge, r. Vick, G. W., K. Urnes, W. S. Kerwin, E. L. Bolson, T. Chung, J. P. Kovalchin, D. J. Sahn, M. Jerosch-Herold, A. H. Stolpen, Three-dimensional shape analysis of right ventricular remodeling in repaired tetralogy of fallot, Am J Cardiol 101 (1) (2008) 107–13. `doi:10.1016/j.amjcard.2007.07.080`.

[95] B. Leonardi, A. M. Taylor, T. Mansi, I. Voigt, M. Sermesant, X. Pennec, N. Ayache, Y. Boudjemline, G. Pongiglione, Computational modelling of the right ventricle in repaired tetralogy of fallot: can it provide insight into patient treatment?, Eur Heart J Cardiovasc Imaging 14 (4) (2013) 381–6. `doi:10.1093/ehjci/jes239`.

[96] L. Zhong, L. Gobeawan, Y. Su, J.-L. Tan, D. Ghista, T. Chua, R.-S. Tan, G. Kassab, Right ventricular regional wall curvedness and area strain in patients with repaired tetralogy of fallot, Am J Physiol Heart Circ Physiol 302 (6) (2012) H1306–H1316. `doi:10.1152/ajpheart.00679.2011`.

[97] D. Chicco, G. Jurman, The advantages of the matthews correlation coefficient (mcc) over f1 score and accuracy in binary classification evaluation, BMC Genomics 21 (1) (2020) 6. `doi:10.1186/s12864-019-6413-7`.

[98] B. R. Cowan, S. M. Peereboom, A. Greiser, J. Guehring, A. A. Young, Image feature determinants of global and segmental circumferential ventricular strain from cine cmr, JACC Cardiovasc Imaging 8 (12) (2015) 1465–1466. `doi:10.1016/j.jcmg.2014.10.005`.

[99] G. J. Wehner, L. Jing, C. M. Haggerty, J. D. Suever, J. Chen, S. M. Hamlet, J. A. Feindt, W. Dimitri Mojsejenko, M. A. Fogel, B. K. Fornwalt, Comparison of left ventricular strains and torsion derived from feature tracking and dense cmr, J Cardiovasc Magn Reson 20 (1) (2018) 63. `doi:10.1186/s12968-018-0485-4`.

[100] F. H. Sheehan, E. L. Bolson, H. T. Dodge, D. G. Mathey, J. Schofer, H. W. Woo, Advantages and applications of the centerline method for characterizing regional ventricular function, Circulation 74 (2) (1986) 293–305. `doi:10.1161/01.cir.74.2.293`.

[101] M. K. Friedberg, F. P. Fernandes, S. L. Roche, C. Slorach, L. Grosse-Wortmann, C. Manlhiot, C. Fackoury, B. W. McCrindle, L. Mertens, P. F. Kantor, Relation of right ventricular mechanics to exercise tolerance in children after tetralogy of fallot repair, Am Heart J 165 (4) (2013) 551–7. `doi:10.1016/j.ahj.2012.06.029`.

[102] L. Jing, C. M. Haggerty, J. D. Suever, S. Alhadad, A. Prakash, F. Cecchin, O. Skrinjar, T. Geva, A. J. Powell, B. K. Fornwalt, Patients with repaired tetralogy of fallot suffer from intra- and inter-ventricular cardiac dyssynchrony: a cardiac magnetic resonance study, Eur Heart J Cardiovasc Imaging 15 (12) (2014) 1333–43. `doi:10.1093/ehjci/jeu123`.

[103] D. Tang, H. Zuo, C. Yang, Z. Wu, X. Huang, R. H. Rathod, A. Tang, K. L. Billiar, T. Geva, Comparison of right ventricle morphological and mechanical characteristics for healthy and patients with tetralogy of fallot: An in vivo mri-based modeling study, Mol Cell Biomech 14 (3) (2017) 137–151. `doi:10.3970/mcb.2017.014.137`.

[104] S. Stephensen, K. Steding-Ehrenborg, P. Munkhammar, E. Heiberg, H. Arheden, M. Carlsson, The relationship between longitudinal, lateral, and septal contribution to stroke volume in patients with pulmonary regurgitation and healthy volunteers, Am J Physiol Heart Circ Physiol 306 (6) (2014) H895–903. `doi:10.1152/ajpheart.00483.2013`.

[105] A. Kovács, B. Lakatos, M. Tokodi, B. Merkely, Right ventricular mechanical pattern in health and disease: beyond longitudinal shortening, Heart Fail Rev 24 (4) (2019) 511–520. `doi:10.1007/s10741-019-09778-1`.

[106] T. Geva, B. Mulder, K. Gauvreau, S. V. Babu-Narayan, R. M. Wald, K. Hickey, A. J. Powell, M. A. Gatzoulis, A. M. Valente, Preoperative predictors of death and sustained ventricular tachycardia after pulmonary valve replacement in patients with repaired tetralogy of fallot enrolled in the indicator cohort, Circulation 138 (19) (2018) 2106–2115. `doi:10.1161/circulationaha.118.034740`.

[107] S. Kollar, E. Balaras, L. J. Olivieri, Y. H. Loke, F. Capuano, Statistical shape modeling reveals the link between right ventricular shape, hemodynamic force, and myocardial function in patients with repaired tetralogy of fallot, Am J Physiol Heart Circ Physiol 323 (3) (2022) H449–h460. `doi:10.1152/ajpheart.00228.2022`.

[108] F. Li, Y. G. Chen, G. H. Yao, L. Li, Z. M. Ge, M. Zhang, Y. Zhang, Usefulness of left ventricular conic index measured by real-time three-dimensional echocardiography

to predict left ventricular remodeling after acute myocardial infarction, Am J Cardiol 102 (11) (2008) 1433–7. `doi:10.1016/j.amjcard.2008.07.034`.

[109] A. Ghai, C. Silversides, L. Harris, G. D. Webb, S. C. Siu, J. Therrien, Left ventricular dysfunction is a risk factor for sudden cardiac death in adults late after repair of tetralogy of fallot, J Am Coll Cardiol 40 (9) (2002) 1675–80. `doi:10.1016/s0735-1097(02)02344-6`.

[110] C. S. Broberg, J. Aboulhosn, F. P. Mongeon, J. Kay, A. M. Valente, P. Khairy, M. G. Earing, A. R. Opotowsky, G. Lui, D. R. Gersony, S. Cook, J. G. Ting, G. Webb, M. Z. Gurvitz, Prevalence of left ventricular systolic dysfunction in adults with repaired tetralogy of fallot, Am J Cardiol 107 (8) (2011) 1215–20. `doi:10.1016/j.amjcard.2010.12.026`.

[111] G. P. Diller, A. Kempny, E. Liodakis, R. Alonso-Gonzalez, R. Inuzuka, A. Uebing, S. Orwat, K. Dimopoulos, L. Swan, W. Li, M. A. Gatzoulis, H. Baumgartner, Left ventricular longitudinal function predicts life-threatening ventricular arrhythmia and death in adults with repaired tetralogy of fallot, Circulation 125 (20) (2012) 2440–6. `doi:10.1161/circulationaha.111.086983`.

[112] S. Orwat, G. P. Diller, A. Kempny, R. Radke, B. Peters, T. Kühne, D. Boethig, M. Gutberlet, K. O. Dubowy, P. Beerbaum, S. Sarikouch, H. Baumgartner, Myocardial deformation parameters predict outcome in patients with repaired tetralogy of fallot, Heart 102 (3) (2016) 209–15. `doi:10.1136/heartjnl-2015-308569`.

[113] S. Kallhovd, J. Sundnes, S. T. Wall, Sensitivity of stress and strain calculations to passive material parameters in cardiac mechanical models using unloaded geometries, Computer Methods in Biomechanics and Biomedical Engineering (2019) 1–12`doi:10.1080/10255842.2019.1579312`.

[114] J. Aguado-Sierra, A. Krishnamurthy, C. Villongco, J. Chuang, E. Howard, M. J. Gonzales, J. Omens, D. E. Krummen, S. Narayan, R. C. Kerckhoffs, A. D. McCulloch, Patient-specific modeling of dyssynchronous heart failure: a case study, Prog Biophys Mol Biol 107 (1) (2011) 147–55. `doi:10.1016/j.pbiomolbio.2011.06.014`.

[115] A. Krishnamurthy, C. T. Villongco, J. Chuang, L. R. Frank, V. Nigam, E. Belezzuoli, P. Stark, D. E. Krummen, S. Narayan, J. H. Omens, A. D. McCulloch, R. C. Kerckhoffs, Patient-specific models of cardiac biomechanics, J Comput Phys 244 (2013) 4–21. `doi:10.1016/j.jcp.2012.09.015`.

[116] J. Probst, G. P. Diller, H. Reinecke, P. Leitz, G. Frommeyer, S. Orwat, J. Vormbrock, R. Radke, F. de Torres Alba, G. Kaleschke, H. Baumgartner, L. Eckardt, K. Wasmer, Prevention of sudden cardiac death in patients with tetralogy of fallot: Risk assessment and long term outcome, Int J Cardiol 269 (2018) 91–96. `doi:10.1016/j.ijcard.2018.06.107`.

[117] G. A. Holzapfel, R. W. Ogden, Constitutive modelling of passive myocardium: a structurally based framework for material characterization, Philos Trans A Math Phys Eng Sci 367 (1902) (2009) 3445–75. `doi:10.1098/rsta.2009.0091`.

[118] A. Krishnamurthy, C. Villongco, A. Beck, J. Omens, A. McCulloch, Left ventricular diastolic and systolic material property estimation from image data: Lv mechanics challenge, Stat Atlases Comput Models Heart 8896 (2015) 63–73. `doi:10.1007/978-3-319-14678-2_7`.

[119] R. Doste, D. Soto-Iglesias, G. Bernardino, A. Alcaine, R. Sebastian, S. Giffard-Roisin, M. Sermesant, A. Berruezo, D. Sanchez-Quintana, O. Camara, A rule-based method to model myocardial fiber orientation in cardiac biventricular geometries with outflow tracts, Int J Numer Method Biomed Eng 35 (4) (2019) e3185. `doi:10.1002/cnm.3185`.